Methodology for a regional tidal model evaluation, with application to central California

Leslie Rosenfeld [a,*], Igor Shulman [b], Michael Cook [a], Jeff Paduan [a], Lev Shulman [c]

[a] Naval Postgraduate School, Code OC/Ro, Monterey, CA 93943, USA
[b] Naval Research Laboratory, Stennis Space Center, MS, USA
[c] University of New Orleans, New Orleans, LA, USA

ARTICLE INFO

ABSTRACT

Observations from disparate observational assets, including tide gauges, moorings, and high-frequency (HF) radars, were used to depict the tidal variability, and to evaluate model tidal simulations, for a region off central California, including the Monterey Bay. For this study, the hydrodynamic model was forced only with tides derived from a large-scale model for the northeast Pacific Ocean. Homogeneous density, and initially horizontally uniform density stratification, cases were considered. The model successfully reproduced tidal sea-surface height variations within the model domain, as determined by comparisons with sea level or bottom pressure measured at six locations. To achieve tidal currents with realistic amplitudes, as determined from HF radar and moored measurements, it was found that barotropic velocity, as well as sea level, from the large-scale regional tidal model must be included in specifying the open-boundary condition. However, even with such forcing, the model with homogeneous density field under-predicted the semidiurnal and diurnal barotropic currents as estimated from depth-averaged currents measured at 11 locations. In the diurnal frequency band, the observed surface and nearshore depth-averaged currents are likely influenced by meteorological forcing, which was not included in the model.

The HF radar-measured surface tidal currents, both semidiurnal and diurnal, are consistent from year to year and between the winter season and the entire year. Semidiurnal surface tidal currents derived from year-long HF radar measurements do not resemble either the modeled or measured barotropic current fields. Rather, they exhibit amplitudes and small-scale spatial variability indicative of the presence of internal tides, thus indicating that model-derived barotropic tidal currents cannot be validated over large spatial extents using long time series of HF radar-derived surface currents. With initially horizontally uniform vertical density stratification, the model produced surface currents with spatial variability and amplitude range comparable to what was derived from HF radar surface current measurements, but the point by point comparisons are not impressive for this region of complex topography. Likewise, the subsurface current comparisons, performed at four deepwater locations, show considerable model-data differences. Possible reasons for these disparities include the effects of atmospheric forcing, spatially and temporally varying stratification, remotely generated coastally trapped waves, and remotely generated internal tides.

Published by Elsevier Ltd.

1. Introduction

Tidal processes, including currents, mixing, and changes in the vertical structure of temperature, salinity, and density, are significant in many littoral regions. Even in areas where the barotropic tidal currents are weak, internal tides may be a large contributor to velocity variance, and they can have significant impact on operations in the littoral zone. Furthermore, internal, or baroclinic, tidal currents can be very difficult to predict since they are highly dependent on bathymetry and stratification, and vary over spatial scales of just a few kilometers.

Even though barotropic tidal currents in the Monterey Bay area are relatively small, baroclinic tidal currents can be an order of magnitude larger ($15-30\,cm\,s^{-1}$, Paduan and Cook, 1997; Petruncio et al., 1998; Petruncio, 1993), and are comparable in magnitude to those associated with California Current eddies and meanders (e.g., Ramp et al., 1997; Strub and James, 2000; Chereskin et al., 2000) and local coastal upwelling jets (Rosenfeld

* Corresponding author.
E-mail address: lkrosenf@nps.edu (L. Rosenfeld).

et al., 1994). The tidal currents often exceed wind-driven currents (e.g., Chereskin, 1995).

Tidal sea-surface height (SSH) variations, and the barotropic tidal currents due to them, are largely deterministic. Baroclinic tidal currents, which depend on stratification that changes over time, likely are not. So, while it is relatively easy to assess the accuracy of model predictions of tidal height, it is difficult to validate tidal current predictions. Observations at a number of locations and depths must be available simultaneously, the model must have a realistic representation of the coincident stratification, and the tidal currents in the observations must be unambiguously separated from currents due to other forcing mechanisms. Xing and Davies (1998a) and Holloway (2001) have previously noted the increased difficulty in validating models of the internal tide, as compared to the barotropic tide. Even comparison of model-predicted barotropic tidal currents with observations is tricky for stratified waters, since long velocity records throughout the water column at a number of locations (although not simultaneous in time) are needed for the "observed" barotropic currents, using traditional methods. Since this type of data coverage is not available for many locations, we were motivated to test another method to estimate the barotropic currents from a more widely available data source: surface currents derived from high-frequency (HF) radar. If the baroclinic tidal currents are highly variable over time, then long time series of currents at a single depth might give a reasonable estimate of the barotropic tidal current. That hypothesis is tested here for the area around Monterey Bay.

2. Background

Regional barotropic tidal models, including some three-dimensional (3-D) ones (e.g., Davies et al., 1997; Foreman and Thomson, 1997), have been implemented in many coastal areas of the ocean. The fidelity of the results from these has generally been quantified using comparison to sea level and bottom pressure signals, but there are exceptions where comparisons to extensive current measurements have also been made (e.g., Davies et al., 1997). In regions where significant vertical density stratification is present, the calculation of barotropic tidal currents from observations is non-trivial. Generally, it is accomplished by the depth averaging of moored current measurements with high vertical resolution and nearly full water-column coverage. (This method is not perfect, however, since rarely are the very near-bottom and near-surface portions of the water column sampled; the effects of bottom friction are ignored; and it assumes the baroclinic tidal signal averages to zero over depth, which is not exactly true over steep bottom slopes or in regions very close to internal tide generating sites.) Long time series of such measurements are needed to resolve unambiguously the major tidal constituents. The paucity of these sorts of records in most of the coastal ocean means that comparison of model currents can usually be done at only a few, if any, locations within the domain.

There are relatively few baroclinic regional tidal models of open coastal areas[1]; Cummins and Oey (1997, northern British Columbia) being among the first, followed by Xing and Davies (1998a, Malin–Hebrides shelf), Holloway (2001, Australian North West shelf) and Pereira et al. (2002, Weddell Sea). Since these models are capable of producing baroclinic currents, one could compare the measured tidal currents directly with those output by the model, without worrying about the barotropic velocity field; but then it would be difficult to know where to attribute any

discrepancies found—i.e. to under-resolved bathymetry, inaccuracies in the forcing, unrealistic stratification, etc. A step-wise approach of first examining the sea-level response, then the barotropic currents which depend on the pressure (sea level) gradient and are sensitive to bathymetry and coastline orography, and finally the baroclinic currents, which depend on the barotropic currents, bathymetry, and stratification, can more reliably allow one to identify where problems are arising.

Some very simple tide models have been applied to Monterey Bay in the past (Lazanoff, 1971; Schomaker, 1983; Petruncio et al., 2002) and, in addition, there are global and regional barotropic tidal models that include this area. The tide in Monterey Bay essentially co-oscillates (Petruncio et al., 1998), so prediction of the sea level to within a few cm and a few minutes is readily achievable. The M_2 (12.42 h) and K_1 (23.93 h) are the largest and second largest constituents, respectively. Freely propagating (i.e. not trapped against a boundary) internal waves must have a period less than the inertial period. The inertial period in Monterey Bay is about 20 h. Therefore, semidiurnal tides are in the internal wave pass-band in Monterey Bay, but the diurnal tides are not. The estimated barotropic tidal currents, although they exhibit significant horizontal variation due to complex bathymetry, are at most only a few cm s^{-1} in most of the area (Petruncio et al., 1998; Lien and Gregg, 2001). The baroclinic tidal currents are much larger and contribute significantly to the kinetic energy, as well as producing a highly variable density field. In fact, within the canyon, semidiurnal frequency currents dominate the power spectra (Xu et al., 2002; Rosenfeld et al., 1999).

The intermittency of the internal tide signal has been noted on many of the world's continental shelves (Baines, 1986). It is also commonly found that the internal tide is not phase-locked to the surface tide, leading to spreading of the internal tide energy into a band around the astronomical forcing frequencies. In Monterey Bay, for example, previous work has shown the baroclinic tidal currents to be highly variable in both time and space (Petruncio et al., 1998; Kunze et al., 2002; Carter et al., 2005). It is possible that these properties of the internal tide may allow barotropic tidal currents to be estimated from very long records of currents at only one depth, even in areas where internal tides are known to be large (Noble et al., 1987). This hypothesis is tested here using long records of surface currents measured by a network of HF radar systems. Increasingly, these systems are being used for mapping surface currents over large parts of the coastal ocean.

3. Model

The model used in this study is the hydrodynamic model of the central California coast developed within the framework of the Innovative Coastal-ocean Observing Network (ICON) project. The ICON model (Shulman et al., 2002) is a 3-D, free-surface, sigma-coordinate version of the Princeton Ocean Model (POM, Blumberg and Mellor, 1987). The orthogonal, curvilinear grid has variable resolution in the horizontal, ranging from 1 to 4 km. The model has 30 vertical sigma levels. Sub-grid scale turbulence is specified using the schemes of Mellor and Yamada (1982) in the vertical and Smagorinsky (1963) in the horizontal. The momentum fluxes at the bottom are determined by the bottom stress. The bottom stress is determined by matching velocities with the logarithmic law of the wall (Tennekes and Lumley, 1972). The bathymetry used in this study has horizontal resolution of approximately 0.01°. The shallowest model depth is 10 m.

Originally, the ICON model was designed for studies of mesoscale variability, including eddies and upwelling filaments, in the Monterey Bay area. As such, the model was one-way

---

[1] Although called a bay, Monterey Bay has fairly unrestricted exchange with the open ocean.

Table 1
Attributes of the five ICON model runs with tidal forcing that are used to assess the effects of different boundary and stratification conditions on the tidal sea level and current signals

Run	Density	Open-boundary condition	Length of run
1	Stratified	Flather	56 d, last 34 analyzed
2	Stratified	Reid and Bodine	56 d, last 34 analyzed
3	Homogeneous	Reid and Bodine	56 d, last 34 analyzed
4	Homogeneous	Flather	56 d, last 34 analyzed
5	Stratified	Flather	402 d, last 380 analyzed

The two types of open-boundary condition are explained in Appendix A.

coupled to a larger-scale regional model of the California Current, surface forcing derived from a fine resolution atmospheric model was applied, and HF radar-derived surface currents were assimilated (Shulman et al., 2002; Ramp et al., 2005; Paduan and Shulman, 2004). In the present study, the ICON model has only tidal forcing to facilitate the identification of issues related to the modeling and evaluation of tidal processes. Atmospheric forcing, realistic stratification, and mesoscale variability all may influence the propagation and generation of internal tides; and ultimately all should be included together with tidal forcing for realistic model predictions. In Shulman and Paduan (2008) the impact of assimilation of HF radar surface currents on the ICON model predictions are investigated. In that paper, atmospheric forcing and coupling to the larger-scale Pacific West Coast model are included into the ICON model forcing. Building on the work presented here, Wang et al. (2008) have taken steps in that direction by adding tidal forcing to a nested implementation of the Regional Ocean Modeling System (ROMS) with the inner nest over Monterey Bay.

In this study, tidal forcing is introduced into the ICON model through specification of the open-boundary conditions described in Appendix A, using the tidal constants interpolated from the Oregon State University Tidal Solution (Egbert and Erofeeva, 2002) for the US West Coast (with 1/12° resolution) to the ICON grid.[2] The OSU solution best fits, in a least-squares sense, the Laplace tidal equations and along-track-averaged SSH data from the TOPEX/Poseidon altimeter. The ICON model is run for 56 d starting August 1, 2000 0100 GMT with the tidal forcing ramping up over the first seven inertial periods. Tidal analysis is performed on the last 34 d, so P_1 is inferred from K_1, and K_2 is inferred from S_2. Inference parameters are based on sea-level analyses. For comparison, a single 402-d model run starting at the same time as the others is included. Tidal analysis on the last 380 d of this long run does not require any inference to resolve the frequencies of the eight forcing constituents.

Results from five case studies (Table 1) are discussed here. A homogeneous density case and an initially horizontally uniform stratified case, with vertical structure typical of summertime conditions, have been run with the Flather (1976) boundary condition (Appendix A, Eq. (2)), and the Reid and Bodine (1968) boundary condition (Appendix A, Eq. (2) with $\overline{u_n^o} = 0$). The initial stratification (Fig. 1) is allowed to evolve in time following the usual POM prognostic equations. The long model run (5) is carried out for the stratified case with Flather boundary condition, and is the only run for which subsurface currents are analyzed.

Surface and subsurface velocity, calculated on an Arakawa C-grid, are interpolated to the center of the grid boxes, and
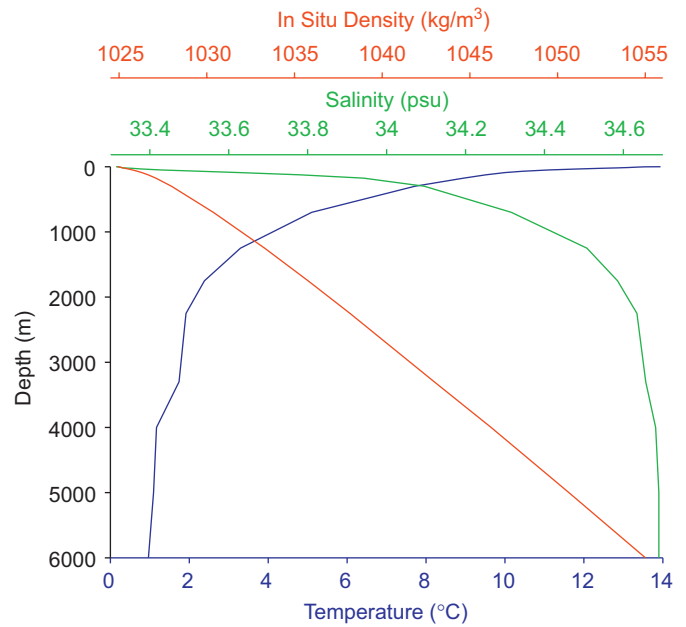

Fig. 1. Initial density, salinity, and temperature stratification used for model runs 1, 2, and 5.

interpolated from the sigma levels to a set of standard depths (0, 10, 20, 30, 50, 75, 100, 125, 150, 200, 250, 300, 400, 500, 600, 700, 800, 900, 1000, 1100, 1200, 1300, 1400, 1500, 1750, 2000, 2500, 3000, 4000, 5000 m). Velocities are also rotated from the native curvilinear grid to an orthogonal N–S, E–W coordinate system.

4. Data

4.1. Sea level and bottom pressure

NOAA's National Ocean Service (NOS) has published tidal constants for three coastal stations on Monterey Bay: Monterey, Moss Landing and Santa Cruz (Fig. 2; Table 2). For the Monterey reference tidal station, the tidal constants for the eight constituents we are interested in are based on a mean of four 1-year analyses (1993–1996). These eight constituents make up over 99% of the sea-level variance at Monterey (Table 3). No augmentation of the constituent amplitudes to account for residual variance was applied to the constituents for this reference station, as is sometimes done to improve the predicted tides (Gill and Ehret, personal communication). Therefore, the constants are truly representative of the purely astronomical tide.

We were able to obtain bottom pressure records from three offshore stations (Fig. 2; Table 2). The tidal amplitudes for these are reported as sea-level height, to be consistent with the coastal stations. We estimate there could be an error of approximately 1% associated with the conversion from bottom pressure to sea-level height.

4.2. Surface currents from HF radar

Two year-long (or nearly so) records of hourly surface current vectors from Monterey Bay were chosen for tidal analysis from a multi-year, though with gaps, set of data derived from HF surface radars. The more recent data (23 July 2003–30 June 2004) makes use of the newer and additional CODAR/Seasonde systems, so has

---

[2] OSU supplied us with a custom domain that extended further south than their TPXO.6 era (version numbers apply to the global solution) regional West Coast solution.
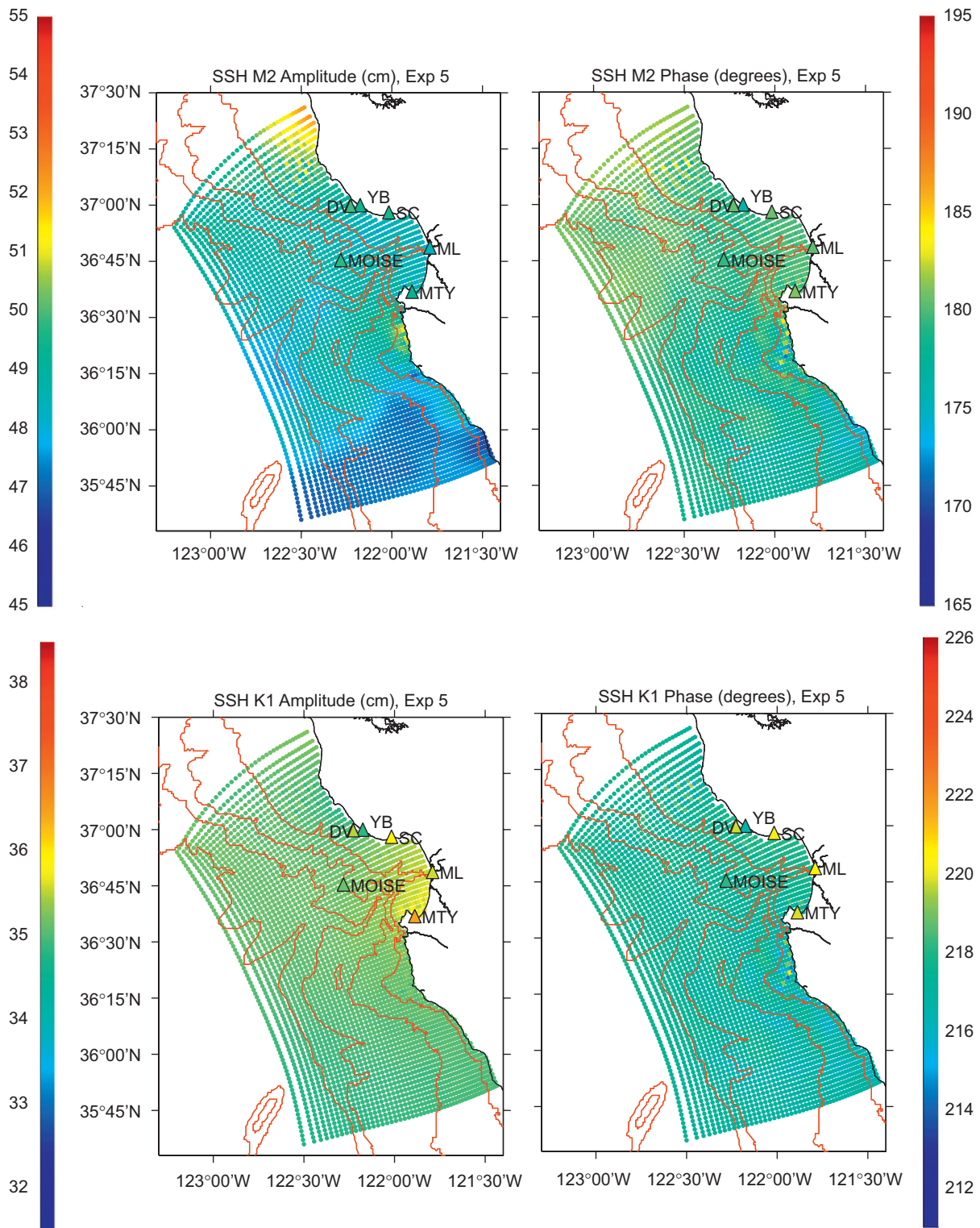
Fig. 2. M_2 and K_1 amplitude and phase for model run 5 and measured sea level. For amplitude, the color bar covers a range $\pm 10\%$ of the mid-value. The phase range corresponds to about 1 h in time. The 200, 1000, 2000, 3000 and 4000 m isobaths are shown. Bathymetry contours on figures are not from actual model bathymetry.

much better domain coverage than the earlier data (1999). In addition, we analyzed the surface current data from the winters, December through February, of 1999–2000, 2000–2001, and 2003–2004. The first and last of these winter records were 2184 h long, while the middle one, which did not include a leap year, was 2160 h long.

4.3. Moored currents

Nearly full-water-column velocity profiles for 29 d or longer are available from eight locations within the model domain: Hopkins Marine Station, Terrace Point (TPT), Sand Hill Bluff (SHB), Davenport, AOSN2, P1, M0, and TRBM. A 14-d ADCP record is

Table 2
Location, depth, and time of sea-level and bottom pressure data used in this study

Variable	Location	Depth	Record length	Dates
Sea level	Santa Cruz (SC) 36°57.5′W 122°01.0′W	Coast	NOS published constants	
Sea level	Monterey (MTY) 36°36.3′N 121°53.3′W	Coast	NOS published constants	
Sea level	Moss Landing (ML) 36°48.1′N 121°47.4′W	Coast	NOS published constants	
Bottom pressure	Yellow Bank (YB) 1 36°59.40′N 122°10.47′W	12 m	63 d	05/07/98–07/09/98
Bottom pressure	Yellow Bank (YB) 2 36°59.40′N 122°10.47′W	12 m	34 d	10/22/98–11/25/98
Bottom pressure	Davenport (DV) 1 37°0.14′N 122°12.90′W	44 m	234 d	09/03/97–04/25/98
Bottom pressure	Davenport (DV) 2 36°58.37′N 122°14.64′W	83 m	137 d	04/02/98–08/17/98
Bottom pressure	MOISE 36°44.76′N 122°16.94′W	1025 m	91 d	06/11/97–09/10/97

Tidal constants shown for Davenport and Yellow Bank locations are averages over the two deployments from each of these sites.

Table 3
Amplitude and percent of total sea-level variance for the eight tidal constituents considered in this study

Constituent	Amplitude (cm)	% Variance
M2	49.3	51
S2	13.0	3.5
K1	36.5	28
O1	23.0	11
N2	11.2	2.6
K2	3.7	0.3
P1	11.4	2.7
Q1	4.1	0.4
Sum of variance		99.50

The amplitudes are those published by the National Ocean Service for Monterey. The calculation of percent variance represented by each constituent uses the average total measured sea-level variance at Monterey from two year-long time series, 1997 and 2000.

available from AOSN1 (Table 4). Multi-year current records at multiple depths distributed over the water column are available for another two locations off Pt. Sur: P2 and P3.

Multi-year upper water-column velocity profiles are available at M1 and M2, and subsurface velocities at a few deeper depths at S2 (very close to M2). Velocity data from the slack surface moorings, M1 and M2, have been corrected for horizontal mooring motion using information from a GPS mounted on the surface buoy. The shallow M0 mooring exhibits very little wander and does not need mooring motion removed from the horizontal velocity estimates.

5. Methods

Tidal analysis was performed using T_TIDE (Pawlowicz et al., 2002), a least-squares harmonic analysis implemented in Matlab

and based on Foreman's (1977, 1978) programs. The tidal analysis of the observations, which were made over a variety of time periods, included the application of a node factor that adjusts the tidal constants calculated for the particular year(s) in which the measurements were made, to values representative of the mean over the 18.6-year cycle of the regression of the longitude of the Moon's node (NOS 2000). In this way, tidal constants calculated from measurements made in different years may be directly compared. For the purpose of making actual sea-level or current predictions, the model forcing would need to include nodal corrections in the inverse sense to adjust these "mean" tidal constants to the specific time period for which a prediction is desired. Here, since the model forcing was predicted without nodal correction, the model time series were analyzed without nodal correction, so the model tidal constants are representative of the mean of the 18.6-year cycle, as are the tidal constants calculated from the observations.

T_TIDE applies the nodal correction factor to the center of the time series, so for multi-year measurement records, albeit with gaps in some cases, we averaged the tidal constants derived from multiple pieces of 1–1.5 years in length. Arithmetic means were used for the semi-major and semi-minor ellipse axes, and vector averages were used to compute the average orientations and phases. By making each piece at least 366 d, the S_1 (period = 24.00 h) constituent was resolved from the K_1 constituent. For time series less than 183 d in length, P_1 was inferred from K_1 and K_2 from S_2, using inference parameters based on sea-level analyses. The justification for, and the limitations of, inference are discussed in Appendix B. Although tidal constants were calculated for all constituents resolved with a Rayleigh factor of 1 (or slightly less than 1 in the case of time series that were just short of 366 d long), results are shown here only for the two largest, the M_2 and the K_1. These two constituents are significant for all the time series analyzed here. The moored velocity time series had signal-to-noise ratios (equal to the square of the ratio of

Table 4
Location, depth, and time of moored current measurements used in this study

Location	Water depth (m)	Instrument	Measurement depth	Record dates	Record length (d)	Tidal analysis length (d)
P1 36°17.8′N 121°59.5′W	84	ADCP	10 8-m bins from 2 to 74 m	03/01/90–05/12/90	73	73
P2 36°20.0′N 122°10.2′W	800	Aanderaa RCM 8 current meter	100 m	05/11/89–04/28/90	350	
				05/14/90–10/09/90	149	516
				05/15/91–12/31/91	230	230
				04/29/92–11/24/93	575	466
				02/09/94–02/09/95	365	365
		RCM8	150 m	04/21/93–07/29/93	99	99
				02/09/94–02/09/95	365	365
		RCM8	225 m	05/15/91–04/28/92	350	350
		RCM8	350 m	05/11/89–05/01/90	355	355
				05/14/90–02/07/93	998	400; 498
				04/21/93–11/24/93	218	218
				02/09/94–02/09/95	365	365
		RCM 8	500 m	05/11/89–10/09/90	516	516
				05/15/91–04/20/93	707	350; 350
		RCM 8	600 m	04/21/93–11/24/93	218	218
P3 36°20.0′N 122°27.6′W	1800	RCM 8	100 m	12/15/89–04/24/90	130	130
				05/13/90–05/12/91	364	364
		RCM 8	350 m	12/15/89–05/07/90	143	
				05/13/90–05/12/91	362	513
		RCM 8	500 m	12/15/89–04/07/90	113	113
				10/11/90–05/12/91	213	213
		RCM 8	1000 m	05/13/90–07/01/90	49	49
				10/11/90–05/12/91	213	213
AOSN1 36°53.4′N 122°07.5′W	~84	ADCP	17 4-m bins from 15 to 79 m	08/20/00–09/03/00	14	14
AOSN2 36°42.5′N 121°52.5′W	~73	ADCP	15 4-m bins from 12 to 68 m	07/30/03–08/28/03	29	29
TRBM 36°42.0′N 121°56.8′W	100	ADCP	21 4-m bins from 12 to 96 m	07/14/05–08/24/05	41	41
Davenport 37°00.0′N 122°12.7′W	32–39	ADCP	14 2-m bins from ~3 to 31 m	04/01/98–08/25/98	145	145
Hopkins 36°37.3′N 121°54.0′W	18	ADCP	13 1-m bins from 3 to 15 m	04/24/00–07/08/04	1535	513 513 513
Sand Hill 36°58.4′N 122°09.5′W	20	ADCP	15 1-m bins from 3 to 17 m	01/31/01–07/11/04	1260	420 420 420
Terrace Pt. 36°56.7′N 122°04.8′W	18	ADCP	12 1-m bins from 3 to 14 m	04/11/01–07/12/04	1191	397 397 397
M0 36°50.0′N 121°54.2′W	70	ADCP	13 4-m bins from 9 to 61 m	06/01/04–02/28/05	270	270
M1 36°45.0′N 122°02.0′W	~1200	ADCP	53 8-m bins from 16 to 432 m	12/01/99–01/01/01	397	397
M2 36°42.0′N 122°23.0′W	~1800	ADCP	53 8-m bins from 16 to 432 m	05/01/01–05/03/02	367	367
S2 36°40.0′N 122°22.5′W	~1800	ADCP	26 4-m bins from 194 to 294 m	01/25/01–02/04/02	376	376

the ellipse major axis to the estimated error in the ellipse major axis), as calculated by T_TIDE, many times greater than 1. Some were in the hundreds or thousands. The SNR for these two constituents for the HF radar-measured surface currents ranged from 1 to 190. All but a very few locations had SNR exceeding 5.

The depth-averaged current ellipses were calculated as follows. For sites with ADCPs that covered most of the water column, velocity data from all good bins were equally weighted to produce a vertical average, on which the tidal analysis was performed. Where there were long records, we averaged together the tidal constituents calculated from each 1–1.5-year piece. For moorings P2 and P3, which had current meters rather than ADCPs, tidal constants were calculated for each depth for each deployment (with inference if the record was less than 183 d), and then tidal constants were averaged over all pieces and all depths (with equal weighting) to get the depth-averaged tidal ellipse. Visual inspection of the P2 and P3 tidal ellipses from the individual depths revealed only minimal variation over the water column. The phases shown in the current ellipses indicate the direction toward which the current flows at the time of high tide for that constituent at Monterey. The tidal current ellipses calculated from the moored velocity data are compared with model ellipses calculated from the velocities at the closest model grid points.

6. Results

6.1. Sea level

All the model runs are quite successful in reproducing the measured bottom pressure and sea-level tidal signals. T_TIDE was used to predict the sea level at each of the sea level and bottom pressure stations for the time coincident with the last 34 (380)-d of the 56 (402)-d model runs. The standard error over all six stations, the locations of which are shown in Fig. 2, is given in Table 5 for each of the five model runs. These were calculated as

$$\left[\frac{1}{N-n} \sum_{\text{stn}} \sum_{\text{time}} (\eta_{\text{model}} - \eta_{\text{pred}})^2 \right]^{1/2} \qquad (1)$$

where $N = 816\,\text{h} \times 6$ stations; $n = 8$ constituents $\times 2$ tidal constants $\times 6$ stations; $\eta_{\text{model}} = $ sea level from the ICON model, $\eta_{\text{pred}} = $ sea level predicted using T_TIDE with NOS-published (for coastal sea-level stations) or data-derived (for offshore bottom pressure stations) tidal constants. The number of degrees of freedom has been estimated as the total number of data points, N, minus the minimum number of data points, n, needed to determine the tidal constants of interest, also equal to the parameters determined in the least-squares tidal analysis (Emery and Thomson, 1997).

The reduction in standard error for model run 5, versus model run 1, which has the same setup, is due to the longer time series analyzed in the later run. The effect of the model spin-up is greater in the analysis of the shorter model runs, but even so, tidal constants calculated from model run 5 using 34, 183 and 380 d records were almost identical. The model does a slightly better job at matching the observed sea level using the Flather boundary condition, which utilizes both the OSU model sea level and velocity at the open boundary. The inclusion of stratification does

Table 5
Standard error of the model sea level over all six stations, versus that predicted using T_TIDE without nodal corrections with the published (sea level) or data-derived (bottom pressure) tidal constants for the eight constituents used in the model forcing

Model run	Std. error (cm)
1	4.18
2	4.26
3	4.28
4	4.21
5	2.23

very little to change the results. This is evidenced by the fact that the M_2 amplitude and phase for sea level are essentially the same for model runs 1 and 4, while the results from run 2 are essentially the same as for run 3. So the differences in the M_2 tidal constants for sea level between runs 1 and 3 are more due to the different boundary conditions, than the addition of stratification. The same is true for the K_1 constituent. The K_1 sea-level amplitude from runs 2 and 4 are essentially the same as from run 3, which differs slightly from run 1, particularly in the southern part of Monterey Bay. The phases from runs 2 and 3 are nearly equal, while the same is true for runs 4 and 1.

The tidal constants from the model run with stratification and the Flather boundary condition, shown in Fig. 2 for the 380-d analysis, are very close to the observations. The M_2 amplitudes range from 48 to 50 cm over the area covered by the measurement sites, while the K_1 amplitudes are between 34.8 and 36.5 cm. The phases of the M_2 and K_1 constituents are 176–181° and 216–220°, respectively, for the measurement sites, with the model-predicted phases within 1–2° of the observed phases for M_2 and 4° for K_1.

6.2. Currents

6.2.1. Horizontal variations

The observed depth-averaged M_2 tidal currents from 11 locations where velocity was measured throughout the water column are shown together with the tidal current ellipses from the homogeneous model with the Flather boundary condition (Fig. 3). (Note that the model surface currents are shown, but we have confirmed that these are representative of flow throughout the water column, as would be expected in a homogeneous model). The model under-predicts the barotropic current amplitudes estimated from measurements, which are themselves very small (for instance only 2.15 cm s^{-1} at Davenport), but it does accurately capture the offshore decay in depth-averaged M_2 kinetic energy along the Sur Ridge (moorings P1, P2, and P3). The homogeneous model run using the Reid and Bodine boundary condition, produces even weaker currents (not shown) than for model run 4. The addition of stratification dramatically changes both the horizontal (Fig. 4) and vertical structure of the semidiurnal (super-inertial) current field. (The rectilinear east-west current ellipses along the offshore boundary of the domain are due to the fact that the model is forced only with the component of flow orthogonal to the boundary.) The addition of stratification has much less effect on the modeled diurnal (sub-inertial) surface currents (Fig. 5 vs. Fig. 6), and model run 4 is in reasonably good agreement with the observations at the P moorings, where it captures the offshore decay in the K_1 current amplitudes (Fig. 5), as it did with the M_2 constituent (Fig. 3).

The measured surface tidal currents exhibit considerable spatial variation at both the semidiurnal (Fig. 7) and diurnal (Fig. 8) frequencies. The surface tidal current ellipses look very much the same, regardless of which year-long period of HF radar-derived currents is analyzed. For instance in both years, the largest M_2 current ellipses are near the head, and to the south, of Monterey Canyon; the locations at which the direction in which the current rotation changes from clockwise to counter-clockwise are nearly the same; and at most locations the phases are the same in both years. Tidal analysis for three winter periods (December–February), when one would expect weaker stratification, yields M_2 ellipses very similar to those for the two year-long periods. The M_2 surface currents from the homogeneous runs (3 and 4) are very similar to each other and very weak, and look nothing like the tidal ellipses derived from these year-long surface current records. However, the model runs with stratification show speeds and spatial variability comparable to that observed.
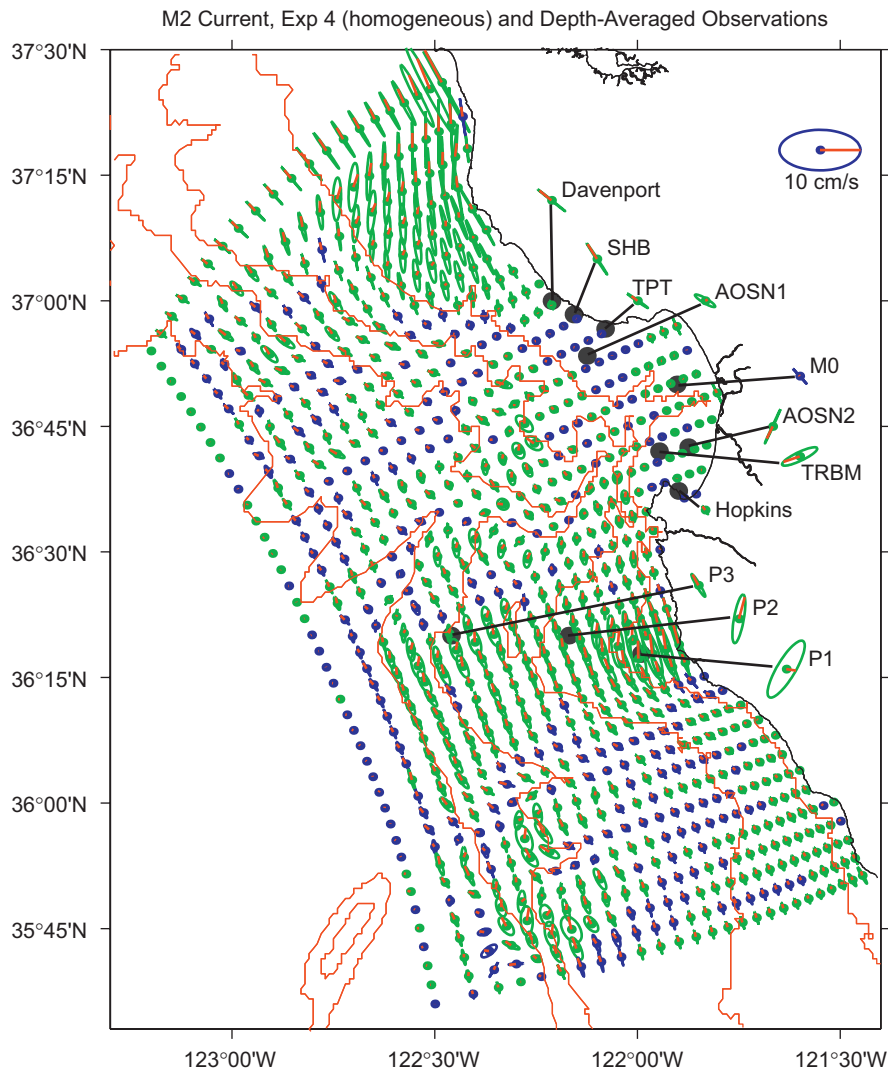
Fig. 3. The depth-averaged M_2 tidal current ellipses for 11 locations (Table 3) are shown, together with the M_2 surface-current tidal ellipses at every other grid point from model run 4, which is homogeneous and uses the Flather boundary condition. Blue ellipses mean the current vector rotates counter-clockwise, green ellipses mean clockwise rotation. The red line in each ellipse indicates the direction toward which current flows at the time of high M_2 sea level at Monterey. The major axis of the scale ellipse in the upper right-hand corner is $10\,\mathrm{cm\,s^{-1}}$. Isobaths are same as in Fig. 2.

One measure of this is that over the same spatial domain, the mean and variance of model run $5\,M_2$ surface current ellipse major axes are 3.4 and $2.5\,\mathrm{cm\,s^{-1}}$, respectively, which are quite close to the 2003–2004 measured values of 3.6 and $3.3\,\mathrm{cm\,s^{-1}}$, while those from model run 4 are only 0.9 and $0.2\,\mathrm{cm\,s^{-1}}$. The stratified model run with Flather boundary condition (Fig. 7) not only achieves current speeds similar to those observed, but also captures some of the details quite well (such as the velocity minima over the canyon and in the northern bight), albeit missing others (such as the phase just north of the canyon inside the bay). The velocity results from run 5, shown here, are very similar to those from run 1.

With the Reid and Bodine boundary condition, the model's K_1 currents (not shown) are very small throughout most of the domain. Even with the Flather condition, the model K_1 surface currents in Monterey Bay are considerably weaker than the measured ones (Fig. 8), although at the southern end of the Bay, the run including stratification and the Flather boundary condition achieves speeds close to those observed. While theoretically, the tidal analysis should resolve the K_1 astronomically forced signal from the S_1 meteorologically forced response in the observed time series, the sea-breeze may not be exactly phase-

locked to the 24-h solar day. Knowing that the energetic diurnal band surface currents are coherent with the local wind (Paduan and Rosenfeld, 1996) and show other evidence of being wind-forced (Paduan and Cook, 1997), and surmising that energy could be leaking into the K_1 period, we tried other methods to separate the diurnal wind driven from tidal currents in the velocity measurements. The K_1 ellipses generated from tidal analysis of just the winter months are similar in size, or larger, than those from the year-long analyses, indicating that, unfortunately, we can not separate the wind driven from astronomical effects by narrowing our focus to certain seasons of the year. We also know that the small K_1 currents in the model are not due to something as simple as incorrect inference values resulting in excessive energy being removed from the K_1 constituent and put into the P_1, since with the 380-d run no inference is needed.

6.2.2. Vertical variations

Over the inner shelf (moorings Davenport, SHB, TPT, and Hopkins), the measured tidal currents are nearly uniform with depth, with the exception of a slight surface enhancement at Davenport, so the depth-averaged ellipses (Figs. 3 and 5) are representative of the tidal currents throughout the water column.
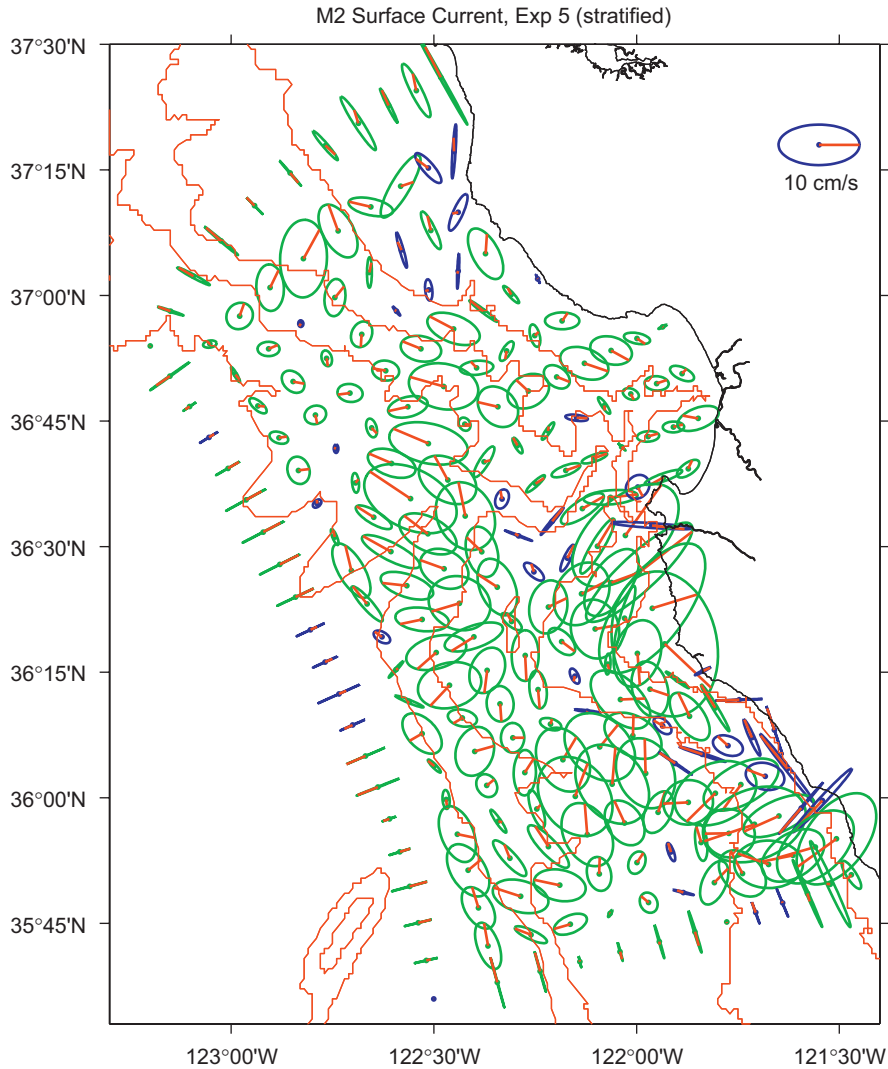
Fig. 4. M_2 surface-current tidal ellipses at every 4th grid point from model run 5, which is stratified and uses the Flather boundary condition. Ellipses from run 1 are virtually identical to those from run 5. Ellipse explanations and bathymetry are as in Fig. 3.

We compared horizontal current ellipses versus depth from the deepwater moorings M1, M2, P2, and P3 (Fig. 9) with the results from model run 5. Record lengths of at least 366 d[3] were used so that the ellipses represent averages throughout the year, thus smoothing over changes due to seasonally varying stratification. The use of time series longer than 183 d avoided having to infer any of the eight tidal constituents used in the model forcing. This is important because we do not have a good way to estimate what the inference parameters should be for the baroclinic tidal currents. For records longer than 366 d, the K_1 and S_1 constituents are also resolved.

Turning our attention first to the diurnal currents at the location of mooring M1, we present the current ellipses derived from data collected during the year 2000, together with the surface ellipses derived from HF radar data collected during 1999 and 2000, and the ellipses at standard depths derived from model run 5 (Fig. 10). Analysis of the moored data for other years is very

consistent with the results shown here. There is also a high degree of similarity between the 1999 and 2000 surface current ellipses as seen in the top row of ellipses in Fig. 10. The top four K_1 current ellipses (8 m bins) exhibit significant clockwise turning (change in orientation) with depth. The top bin, centered at 16 m, is oriented to the right of the surface current ellipse. The surface current ellipses for the both the K_1 and O_1 constituents are about 50% larger than the current ellipses at 16 m (top bin). Below 50 m, the K_1 and O_1 ellipses decay in depth to a minimum amplitude between 200 and 250 m, and then increase uniformly below that to the bottom of the ADCP range at 432 m. Above 200 m, the model K_1 currents are substantially smaller than the measured ones and do not exhibit the turning and decrease in amplitude away from the surface that the observed currents show. Below 250 m, the model ellipses are comparable to, though still weaker than, the observed ones. The S_1 ellipses, at exactly the diurnal period, also exhibit clockwise turning of the orientation over the upper water column, but the surface ellipse is more than three times as large as the one at 16 m depth. The strength of the S_1 signal decays substantially over the top 100 m, and the ellipses are uniformly small below that. No model S_1 current ellipses are shown, since no forcing was applied at this period.

---

[3] At P2 and P3, tidal ellipse parameters were calculated from multiple pieces of the data record and then averaged together. Some of these pieces were shorter than 366 d, but all except three were longer than 183 d (Table 4).
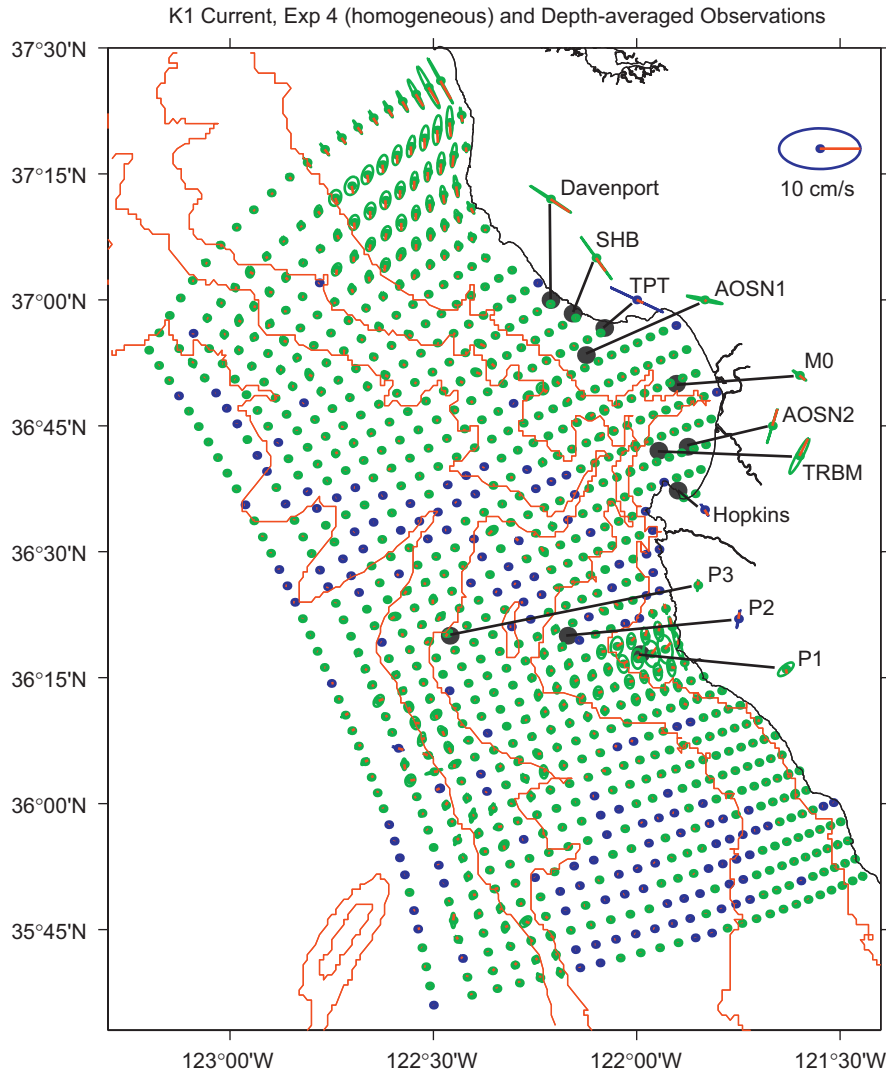
Fig. 5. The depth-averaged K_1 tidal current ellipses for 11 locations are shown, together with the K_1 surface-current tidal ellipses at every other grid point from model run 4, which is homogeneous and uses the Flather boundary condition. Ellipse explanations and bathymetry are as in Fig. 3, except that the red line in each ellipse indicates the direction toward which current flows at the time of high K_1 sea level at Monterey.

The measured and modeled (run 5) K_1 period currents throughout the upper 500 m at M2/S2 are less than $1\,cm\,s^{-1}$ in amplitude, so are not shown here.

The observed M_2 currents (Fig. 11) exhibit substantial vertical, as well as horizontal (compare M1 and M2 moorings) variation, which we have already seen in the HF radar-derived surface current ellipses. M_2 current ellipses from the S2 mooring, available for the ~200–300 m depth range for August 2000–August 2001, are consistent with those measured 4 km away at M2 during May 2001–May 2002, in terms of amplitude, orientation and sense of rotation, but differ in phase by ~75°. The model M_2 currents exhibit only very small differences over the short distance between the two grid points closest to moorings M2 and S2, but exhibit substantial differences over the distance between the M1 and M2 moorings, as well as showing large vertical variability. The range of amplitudes in the model currents is comparable to that observed, but there is little correspondence between the measured and modeled current ellipses at a given location and depth. Note that the surface current ellipses (shown only for the M1 location, since the M2 mooring is beyond the range of the HF radars) are smaller than those at 16 m (top bin).

The K_1 model currents at P2 and P3 are in reasonable agreement with the measured ones (Fig. 12), albeit weaker, with

both model and measured currents showing a slight increase with depth at both locations. Note that the model currents are weaker than the measured ones even at 500 and 1000 m depth 30 nm offshore (P3). Below 300 m, the M_2 model currents are not too dissimilar from the measured ones, but at 100 m (P3) and 150–250 m (P2), the model ellipses are significantly larger. No data are available at these locations to verify the surface intensification seen in the model.

7. Discussion

Our ultimate goal is to accurately predict tidal currents in the central California region, so effects of bathymetry, spatially and temporally variable stratification, wind forcing, and low-frequency currents must be taken into account. Model results with tidal, atmospheric, and remote oceanographic forcing applied may be compared with Eulerian and Lagrangian current measurements, but the tidal component is not separated out. The step-wise approach to model runs and model-data comparisons taken here more easily allows the identification and correction of errors and inaccuracies, before including all the non-tidal forcing. To achieve realistic baroclinic velocities, the model must produce
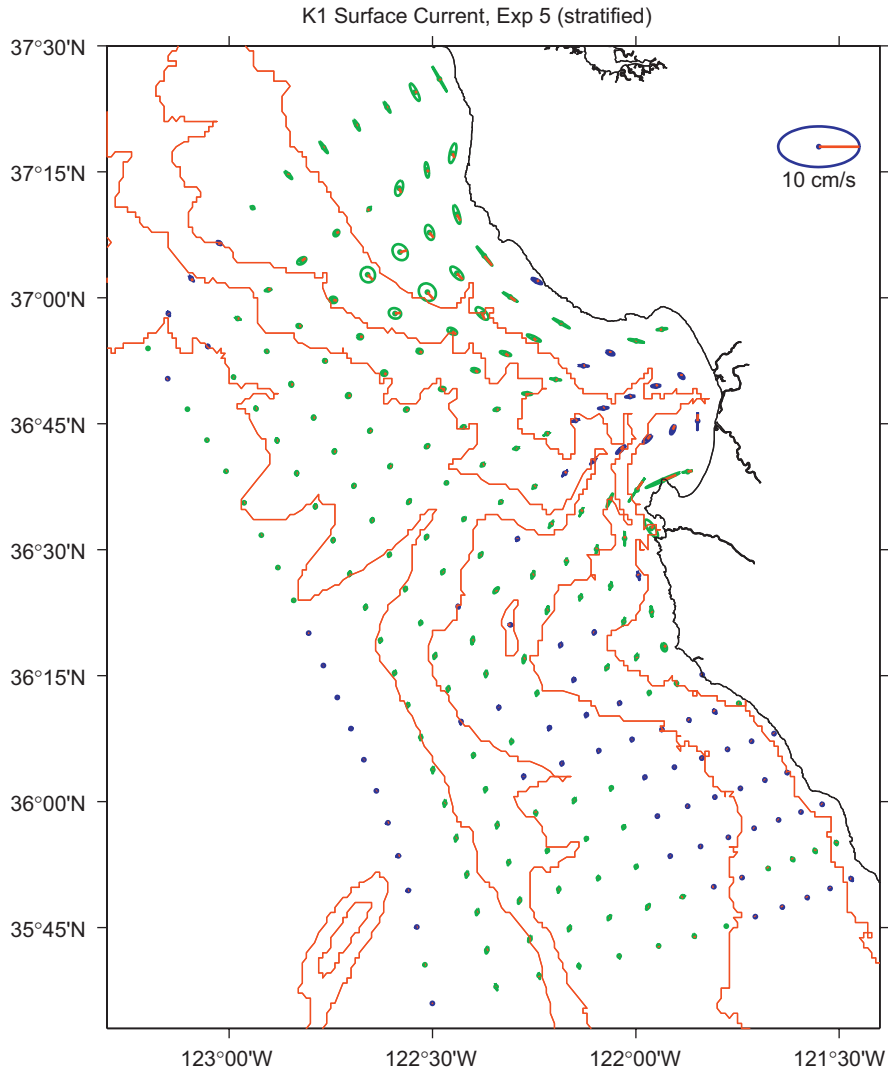
Fig. 6. K_1 surface-current tidal ellipses at every 4th grid point from model run 5, which is stratified and uses the Flather boundary condition. Ellipse explanations and bathymetry are as in Fig. 3, except that the red line in each ellipse indicates the direction toward which current flows at the time of high K_1 sea level at Monterey.

realistic barotropic velocities, and in order to produce "good" barotropic velocities, the model must have an adequate representation of tidal sea level. Hence, we start with the sea-level comparisons, while acknowledging that a model's success at reproducing sea level does not guarantee that the model will represent barotropic tidal currents well. Then, following Cummins and Oey (1997), we compare velocity from a homogeneous case with a summer stratification case.

The approach used in the present study, i.e. forcing only with the predictable barotropic tides, allows for comparison with data collected for many different purposes from many years. As noted by Davies and Xing (1995), the data do not have to be coincident in time with each other or with the model run. Implicit in this approach is the assumption that the majority of the internal tide energy is generated within the model domain. There is observational evidence that supports local generation of internal tides within our model domain. Kunze et al. (2002) concluded from calculations of energy flux that there was a local source for internal tide energy within the canyon inside Monterey Bay, but they were unable to identify the source for up-canyon energy flux at the mouth of the canyon. Carter and Gregg's (2002) energy flux calculations also suggest local internal wave generation throughout the Monterey Canyon.

Carter et al. (2005) present evidence for both local and remote internal tide generation in the Monterey Bay region. Our domain encompasses the sites that Carter et al. (2005) have identified as likely internal tide generation sites for Monterey Bay, including: the shelf break, the canyon rims, within the canyon, and a submarine fan north of the canyon, including depths out to 3500 m.

Kurapov et al. (2003) took a different approach with their efforts to model the internal tides off the coast of Oregon. They also used horizontally uniform stratification and forced with just the barotropic component of velocity on the open boundaries. They assume that the open-boundary conditions are the major source of error in the model, while also noting that the horizontally uniform stratification is a significant deficiency. Their primary model domain encompasses only a portion of the continental shelf and excludes the continental slope—often an area of significant internal tide generation. Without specifying the internal tide along the open boundary of the model, the only way to get that energy into the model domain was through assimilation of data (HF radar-derived surface currents in their case). When they forced a larger model domain, they did produce internal tides of reasonable amplitude at their one comparison site (a moored ADP).
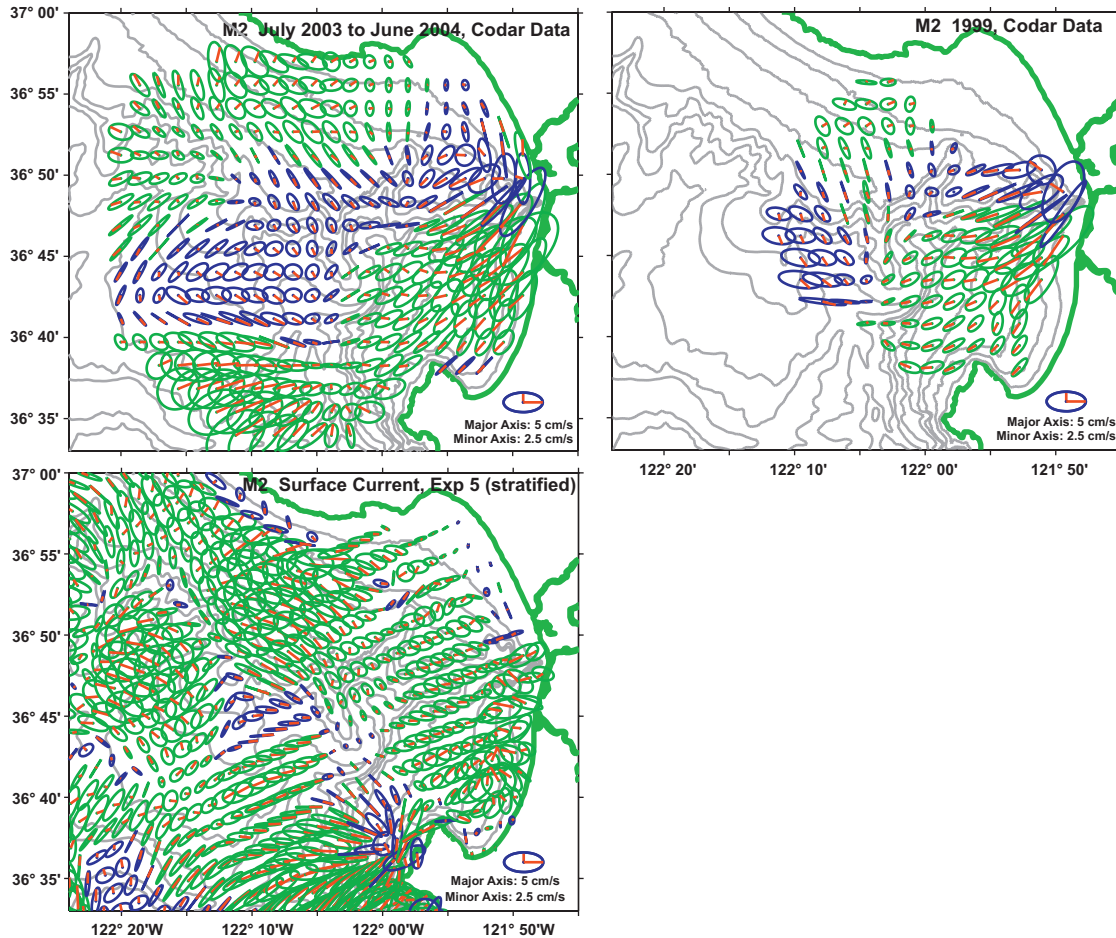
Fig. 7. M_2 surface-current tidal ellipses, derived from velocities measured by the HF radar array during July 2003–June 2004 (top left), 1999 (top right) and from model run 5 (bottom), which is stratified and uses the Flather boundary condition. Measured ellipses are shown only for locations where there was data coverage at least 50% of the time. Only the portion of the model domain which is usually covered by the HF radar array is shown. Ellipse explanations are as in Fig. 3. The 25, 50, 75, 100, 250, 500, 750, 1000, 1500, 2000 and 2500 m isobaths are shown.

7.1. Model variables

Discussion of the interrelated issues of model run length, model record length used for tidal analysis, and the application and validity of tidal inference are included in Appendix B.

7.1.1. Boundary conditions

The model runs with the Reid and Bodine boundary condition produced tidal sea-level oscillations nearly indistinguishable from the model runs using the Flather boundary condition. However, the two boundary conditions produced very different model velocity fields. In the case of the Reid and Bodine boundary condition, i.e. using only the sea level from the OSU model in Eq. (2) (Appendix A), the velocities were unrealistically small. Hence, all subsequent discussion relates to the model runs with the Flather boundary condition.

7.1.2. Stratification

Two simple stratification conditions were chosen for analysis and comparison with data in this study. The surface currents from the homogeneous model runs are compared with the depth-averaged observed velocities (our best estimate of the actual barotropic currents). The total depth-dependent velocities, including both the barotropic and baroclinic components, from the stratified runs are used for comparison with the observed velocities. Although most of the difference between the homogeneous and stratified cases is expected to be due to the baroclinic contribution, there may also be some effect of the stratification on the vertical viscosity. Cummins and Oey (1997) ran the POM for the area off northern British Columbia in the diagnostic mode with stratification, so no internal tide developed, to examine the effect of stratification on vertical viscosity. They found that it was almost identical to the homogeneous case. Xing and Davies (1998a and earlier work by the same authors cited therein) state that changes in the eddy viscosity due to seasonal changes in stratification can produce a phase shift across the pycnocline.

7.2. Sea-surface height

The model is very successful at reproducing the observed tidal SSH (Table 5), although admittedly the available bottom pressure and coastal sea-level measurement sites cover only a small portion of the domain, over which the tidal constants do not exhibit a great deal of variation (Fig. 2). The model SSH is little affected by the choice of boundary condition, or the inclusion of stratification. Note that analysis of 183 d (the record length needed to resolve all eight of the constituents using a Rayleigh criterion of one) from model run 5 produces nearly identical results as for 380 d, so future model runs with a spin-up time of
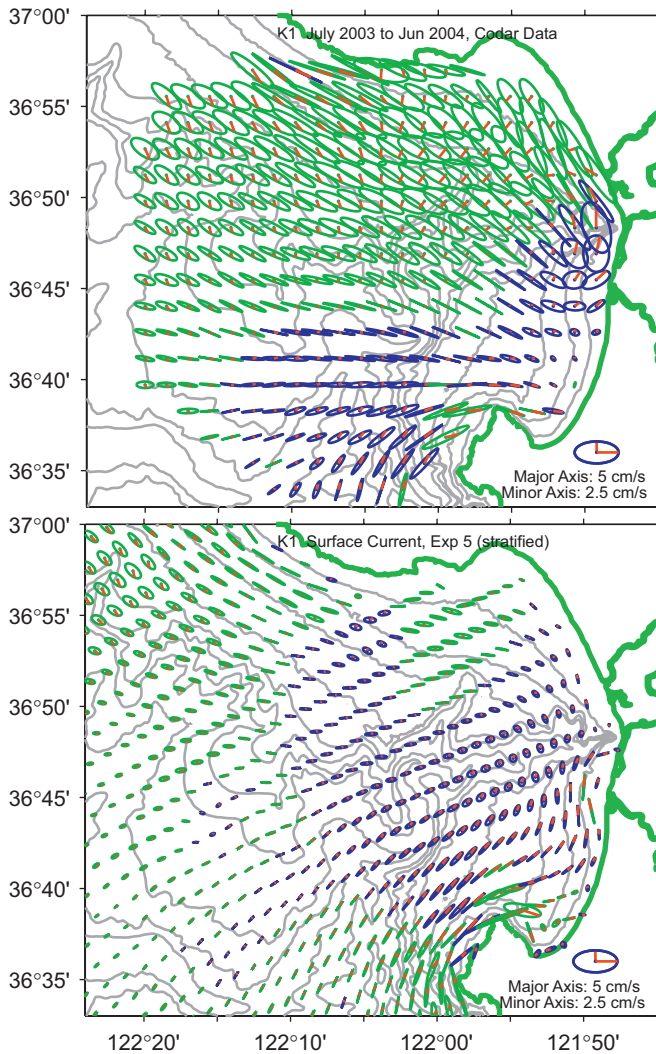
Fig. 8. K_1 surface-current tidal ellipses derived from velocities measured by the HF radar array (top) and from model run 5 (bottom). Measured ellipses are shown only for locations where there was data coverage at least 50% of the time during July 2003–June 2004. Only the portion of the model domain which is usually covered by the HF radar array is shown. Model run 5 is stratified and uses the Flather boundary condition. Blue ellipses mean the current vector rotates CCW, green ellipses mean CW rotation. The red line in each ellipse indicates the direction toward which current flows at the time of high K_1 sea level at Monterey. Isobaths are as in Fig. 7.

1 month followed by a 183-d record for analysis should be sufficient.

7.3. Currents

The observed tidal current ellipses, whether measured by HF radar or from moorings, show remarkable consistency from year to year, and even when comparing one season (winter) to the whole year. This is in contrast to the central Oregon shelf, where Erofeeva et al. (2003) concluded that surface currents measured by HF radar during the winter were sufficiently representative of the barotropic tidal currents to use them for assimilation into a barotropic tidal model, while the summertime surface currents were substantially different. They attributed these seasonal differences, in part, to changes in stratification and wind forcing, including possibly the seabreeze.

The depth-averaged currents from entirely independent measurements, exhibit spatial variability consistent with each other (e.g., compare SHB with Davenport, or AOSN2 with TRBM in Figs. 3 and 5), and with what would be expected based on the bathymetry. The homogeneous model captures some of the observed spatial variability in the barotropic currents, but the model currents are too weak both in the semidiurnal and diurnal bands. When the Reid and Bodine boundary condition is used, the model currents are even weaker than with the Flather boundary condition.

7.3.1. Diurnal currents

At the K_1 period, the observed surface currents in some areas are significantly stronger than those produced by the model. Several factors not included in the model forcing could enhance the observed diurnal period currents. While we have not found a method to separate unequivocally the diurnal tidal currents from diurnal wind driven currents, we do have evidence that much of the K_1 response may be wind driven. The decrease in amplitude and the clockwise turning in the orientation of the ellipses with depth (Fig. 10) are indicative of frictional forcing from above (Faller and Kaylor, 1969; Rosenfeld, 1987). A steady wind stress in combination with a diurnally varying mixed-layer-depth can also produce diurnal current variability (Price et al., 1986). In addition, the depth-averaged K_1 currents are stronger than the M_2 currents on the inner shelf north of the bay (compare Davenport, SHB, TPT, and AOSN1 in Figs. 3 and 5), an area known to have strong diurnal wind forcing (Kindle et al., 2003), as opposed to the situation expected from astronomical tidal forcing which would result in larger M_2 than K_1 barotropic tidal ellipses, as seen at P1, P2, and P3. Most locations where we have top to bottom current measurements are in fairly shallow water where much of water column could be directly influenced by frictional wind forcing. Also, the diurnal wind variability can cause diurnally varying cross-shelf pressure gradients (setup/setdown) resulting in barotropic currents felt throughout the water column (Rosenfeld, 1988). While many of the time series are long enough to resolve the astronomical K_1 from the meteorological S_1 constituent, there is no guarantee that the meteorological forcing is confined to a line in the frequency spectra. Indeed, the wind energy measured at mooring M1 during 2000 is significantly elevated above background levels throughout the 0.042 ± 0.002 cph frequency band. The S_1 ocean response is so large (Fig. 10) that it seems likely that energy would spread into neighboring frequencies.

Another signal that may be contributing to diurnal current variability in the real ocean, but not in the model, is the presence of baroclinic and/or non-tidally forced coastally trapped waves (CTWs) propagating into the area from outside the local domain. These would not necessarily be captured in the model forcing, and could contribute to short length scale variations in the model currents. Erofeeva et al. (2003) found that a regional barotropic tidal model for the Oregon shelf, forced with an earlier version of Egbert's global tidal model, did not reproduce the measured diurnal currents very well, which they attributed to the presence of barotropic CTWs. The K_1 currents measured at 500 and 1000 m depth 30 nm offshore at mooring P3, exceed the model currents there (Fig. 12). The depth and offshore distance make it unlikely that this enhancement is due directly to wind stress or coastal setup/setdown. Although the K_1 period exceeds the inertial period, so no freely propagating internal waves are allowed, the structure of CTWs are somewhat sensitive to the chosen stratification (Crawford and Thomson, 1984; Xing and Davies, 1998b). Any deficiencies in the model's representation of a diurnal CTW will show up more in the velocity than the SSH field (Foreman et al., 1995). Cummins et al. (2000) used the POM to
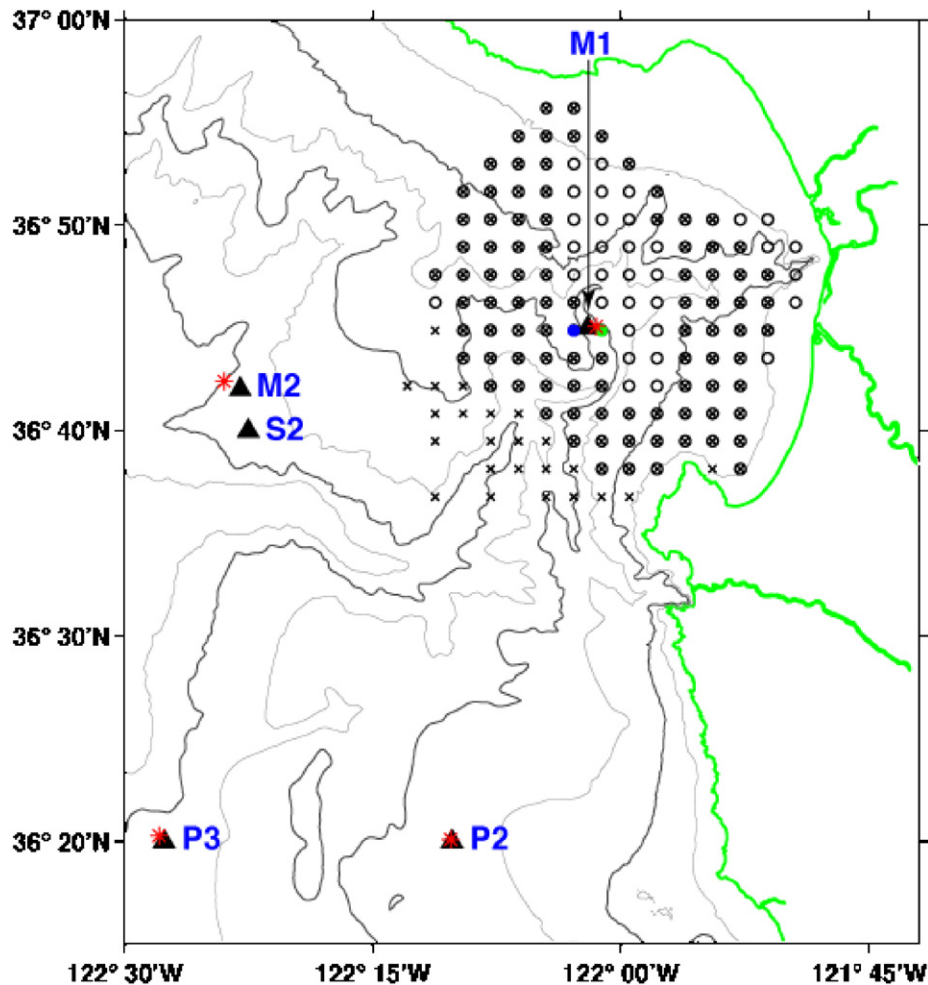
Fig. 9. Map showing moorings (black triangles), HF radar coverage (o: 1999 only, × : 2000 only, ⊗: both 1999 and 2000), and model grid point locations used in subsequent figures. The green and blue solid circles indicate the positions of the HF radar current measurements closest to mooring M1 in 1999 and 2000, respectively. Red asterisks indicate locations of model grid points used for comparison to moored measurements. Dark gray contours are 100, 1000 and 2000 m isobaths. Light gray contours are 50, 500, 1500 and 2500 m isobaths.

consider the effect of stratification on the diurnal tidal currents off Vancouver Island. With the inclusion of stratification, they found greater vertical structure in the currents over the continental slope versus over the shelf, consistent with the structure of CTWs with realistic topography and stratification (Huthnance, 1978).

7.3.2. Semidiurnal currents

The stratified model M_2 currents exhibit large vertical and horizontal variability with realistic spatial scales, and the range of amplitudes is comparable to those observed, but there is little correspondence between the measured and modeled current ellipses at a given location and depth. A number of factors probably contribute to this. Details of the baroclinic tidal currents are likely to be very sensitive to bathymetry (hence model spatial resolution). Recent results from an unstructured non-hydrostatic model, SUNTANS, have demonstrated the necessity of high spatial resolution (sub-kilometer scales in this case) in attaining realistically strong internal tidal currents (Jachec et al., 2006). Cummins and Oey (1997), however, found that in their studies using POM off northern British Columbia, increasing the horizontal resolution from 5 to 2.5 km had little effect, but they used the same topography for both cases (with interpolation for the higher spatial resolution). Also, the shallowest depth in the ICON model is 10 m, and some of the moorings used for comparison

(Terrace Pt., Sand Hill Bluff, and Hopkins Marine Station) were deployed in water depths not much greater than that (18–20 m). Blanton et al. (2004), using a barotropic finite element model to simulate the tides in the South Atlantic Bight, found that inclusion of the estuaries and tidal inlets improved the model accuracy, particularly in its representation of the semidiurnal tides. This was primarily due to changing the reflectance at the coastal boundary of the semidiurnal period inertia-gravity waves propagating cross-shelf. While this could indicate that exclusion of the Elkhorn Slough from the ICON model domain may be a source of error, particularly for the super-inertial semidiurnal tides, the sort of cross-shelf amplification that can occur on the wider East Coast shelves is not likely to be as important a factor on this narrower West Coast shelf.

The specification of the initial stratification is another factor that may influence the detailed structure of the tidal currents. We have taken as a starting point the two simplest cases: a homogeneous density field, and one varying only in the vertical. Of course, in the real ocean, the stratification varies in all three dimensions and is constantly being modified by forces not included in our tidal-only model. For instance in the Japan/East Sea, Park and Watts (2006) found that the generation and propagation of semidiurnal tides were influenced by horizontal gradients in the stratification associated with mesoscale features. In the Monterey Bay region, stratification throughout the water
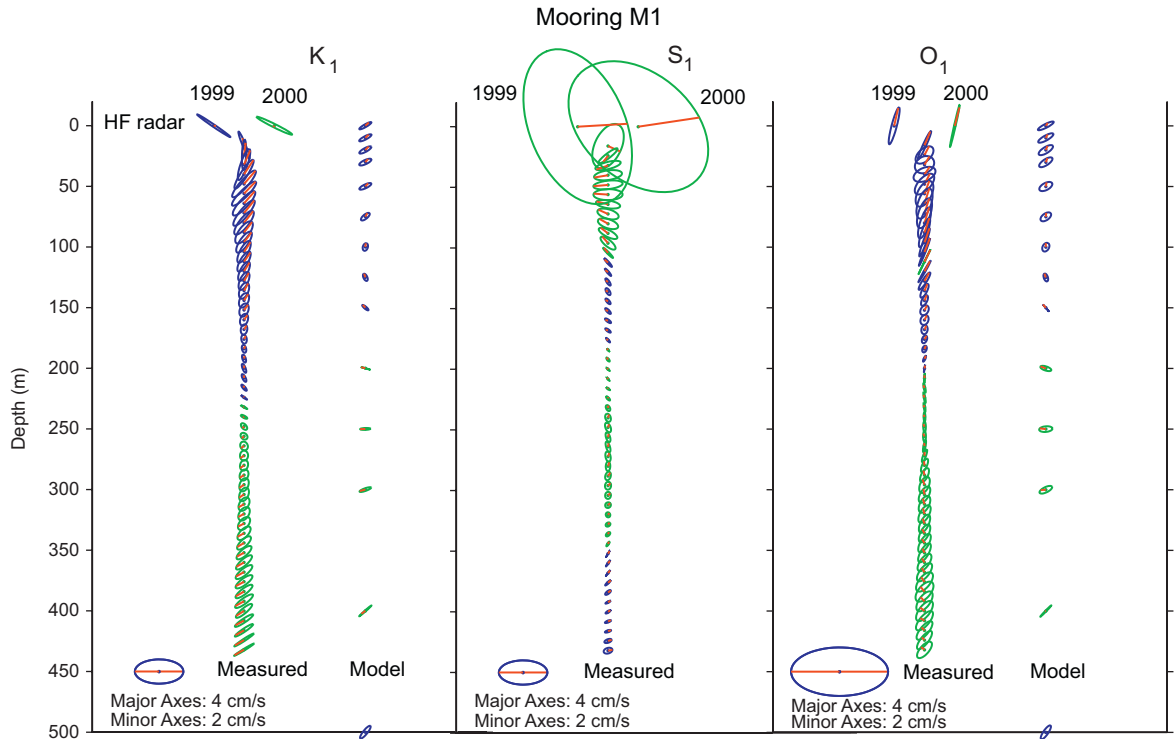
Fig. 10. Horizontal current ellipses (north is up on the page) measured by the ADCP at mooring M1 (12/01/99-01/01/01) and those measured by HF radar (1999 and 2000) at the surface nearby, are compared with the closest currents from model run 5 for the diurnal tidal constituents K_1 (23.93 h), S_1 (24 h), and O_1 (25.82 h). No model ellipses are shown for S_1 since the model is not forced at that frequency. Note that the velocity scale for O_1 is twice that of K_1 and S_1. See Fig. 3 for an explanation of the ellipse colors.
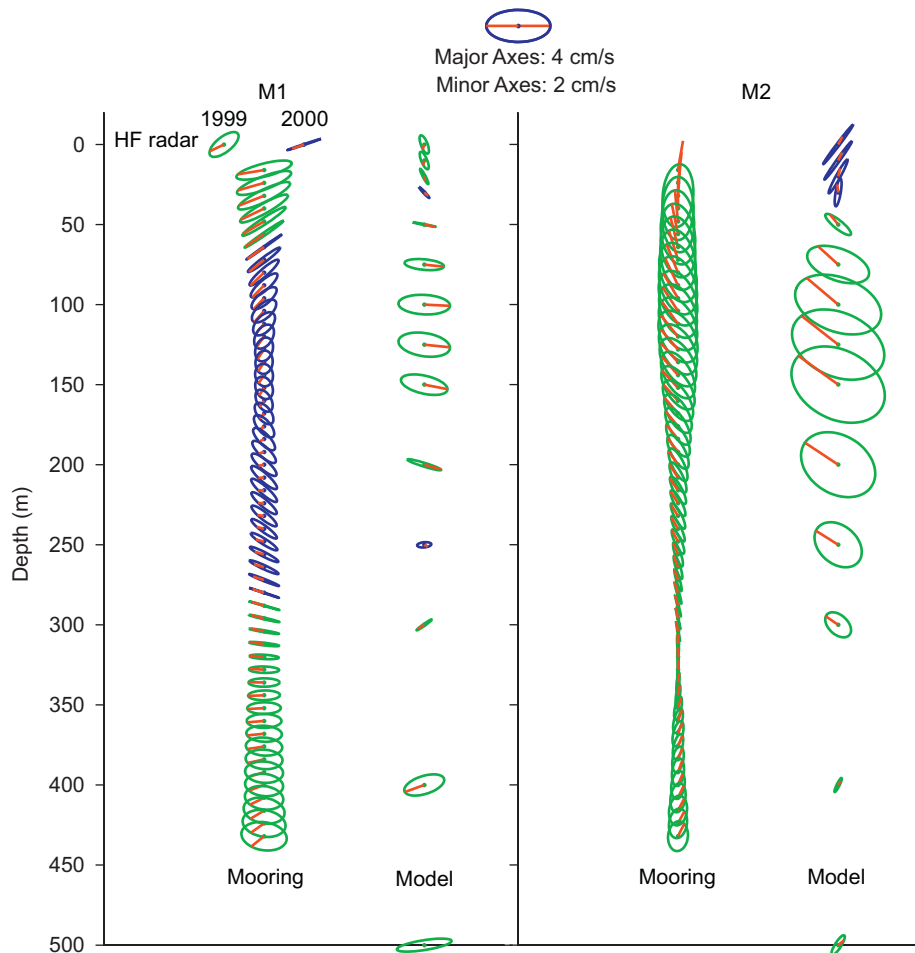

Fig. 11. M_2 (12.42 h) horizontal current ellipses measured by ADCPs at moorings M1 (12/01/99-01/01/01) and M2 (05/01/01-05/03/02) and surface current ellipses measured by HF radar near mooring M1 for 1999 and 2000 (M2 is beyond the HF radar range) are shown next to current ellipses from model run 5 (closest grid point to mooring).
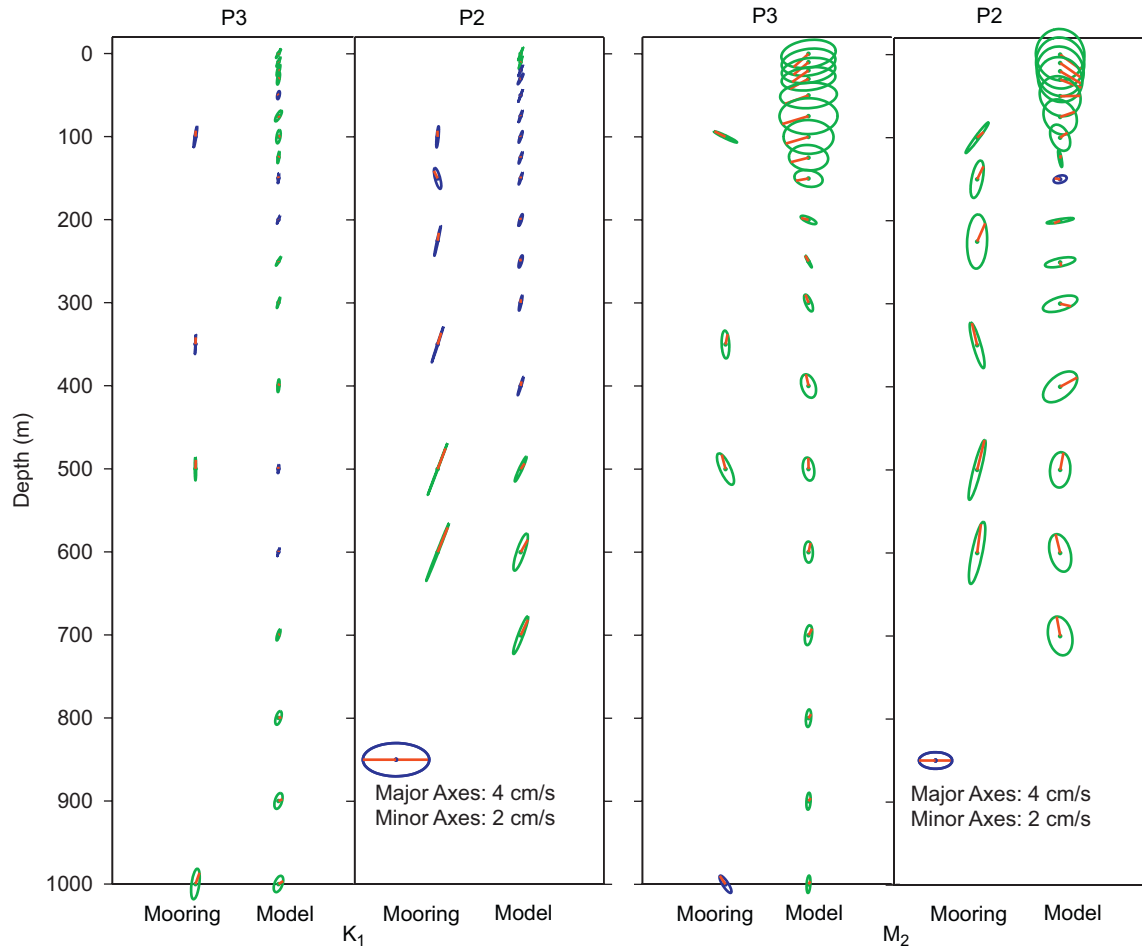
Fig. 12. Measured and modeled (run 5) horizontal current ellipses for K_1 and M_2 constituents at moorings P2 and P3. Note that the velocity scale for the K_1 ellipses is twice that for the M_2 ellipses.

column can change considerably in less than a day, leading to significant changes in both the mixing (Carter and Gregg, 2002) and internal tide regimes (Petruncio et al., 1998). The fact that the semidiurnal tidal surface currents show remarkably consistent spatial patterns year to year, and during the winter versus the whole year, suggests that the spatial pattern may be due more to deep stratification and/or bathymetry, than to the more rapidly varying upper ocean stratification. Xing and Davies (1998a) found that in many areas of the Malin–Hebrides shelf and shelf edge, there was little difference in the internal tide modeled with winter vs. summer stratification.

Yet another possible deficiency in the model could be the fact that it is hydrostatic. We believe that this does not have a major impact on the results at the low-frequency end of the internal wave pass band where we are working. After removal of isopycnal displacements due to the barotropic tidal currents flowing over sloping topography, Kunze et al. (2002) found a kinetic to potential energy ratio of about 2.1, consistent with the theoretical value for hydrostatic internal waves of semidiurnal period.

Finally, our assumption that the majority of the internal tide energy is generated within the model domain may not be correct. Certainly, there is evidence for propagation of low mode internal waves propagating over long distances (Alford, 2003; Rainville and Pinkel, 2006), and the extent to which these waves might influence the internal tide signal within Monterey Bay is unknown.

7.4. Recommendations

One of our motivations in performing this work was the hope that long time series of surface currents could be used to estimate barotropic tidal currents. Semidiurnal surface tidal currents derived from year-long HF radar measurements do not resemble either the modeled or measured barotropic current fields. Rather, they exhibit amplitudes and small-scale spatial variability indicative of the presence of internal tides. This result indicates that model-derived barotropic tidal currents cannot be validated over large spatial extents using long time series of HF radar-derived surface currents. Since it appears that the baroclinic contribution does not cancel out over time, it suggests that long time series of subsurface currents may be used to examine the vertical structure of total (barotropic plus baroclinic) tidal velocities. We have used a few long time series of moored current measurements to compare with baroclinic model results. However, since we initialized the model with a horizontally uniform stratification and there is no buoyancy forcing applied, we can not expect a realistic evolution of the density field, and we would not necessarily expect a good point-by-point comparison at this stage. Therefore, the main reason to look at the total tidal velocities is to get an idea of the amplitudes and the spatial variability compared to what is observed. Logical next steps would be to run the model with a typical wintertime stratification profile, and then add variations in the horizontal.

Another issue to consider in improving the model performance is to adjust the model dissipation by "tuning" the diffusivity. This may not be practical, however, since measurements reveal that the dissipation rates and diapycnal diffusivities are highly variable over space and time in the region (Carter et al., 2005). From microstructure measurements made along a bathymetric ridge on the continental slope just north of Monterey Canyon, Lien and Gregg (2001) found turbulent dissipation varied over two orders of magnitude between ebb and flood tides. There are also changes in the along-canyon spatial distribution of high mixing regions associated with the flood/ebb cycle (Carter and Gregg, 2002). Based on microstructure measurements made within Monterey Canyon, Carter and Gregg (2002) also found that diapycnal diffusivity is quite variable over the fortnightly time scale.

Because of the confounding effects of atmospheric forcing at frequencies very close to the diurnal tidal constituents, it may not be possible to verify independently the accuracy of a tidal model for this, or many, coastal regions. Thus, one modification to consider in the future is to turn on the diurnal period wind stress and heat flux in the model forcing. Additionally, coupling to the larger-scale regional model, also including tidal forcing, may be important to allow CTWs to propagate into the area from outside of the local domain.

Finally, many studies have demonstrated that data assimilation can significantly improve model predictions in coastal areas. In the present study, the HF radar data were used to understand tidal variability in the area, and for evaluation of model tidal simulations. Assimilation of HF radar-derived surface currents might be a powerful tool to improve tidal (Kurapov et al., 2003), as well as subtidal, model predictions (Paduan and Shulman, 2004), but the data range available to date encompasses only a small portion of the domain that must be covered to include important sites of internal tide generation.

8. Conclusions

Observations from disparate observational assets, including tide gauges, moorings, and HF radars, were used to depict the tidal variability, and to evaluate model tidal simulations, for a region off central California, including the Monterey Bay. To facilitate the identification of issues related to the modeling and evaluation of tidal processes, only tidal forcing, applied at the open boundaries, was used in the POM-based hydrodynamic model. The forcing, derived from a large-scale model for the northeast Pacific (Egbert and Erofeeva, 2002), included the eight largest diurnal and semidiurnal constituents. Homogeneous density, and initially horizontally uniform density stratification, cases were considered. The model successfully reproduced tidal SSH variations within the model domain, as determined by comparisons with sea level or bottom pressure measured at six locations. The model SSH results differed little between homogeneous and stratified runs, and between runs using the Reid and Bodine (1968) boundary condition and those using the Flather (1976) boundary condition (Appendix A). The former boundary condition produced very weak tidal currents in comparison to the latter condition, and in comparison with measured tidal currents, which are consistent from year to year and between the winter season and the entire year.

The homogeneous model with the Flather boundary condition produced tidal currents somewhat weaker than the barotropic tidal currents estimated by depth-averaging measured currents throughout the water column at 11 locations within the model domain. The observed cross-shore decrease in tidal current amplitude along the Sur Ridge was reproduced by the model. In contrast to the relationship between M_2 and K_1 amplitudes in SSH, the measured, but not the modeled, K_1 barotropic currents exceed the M_2 barotropic currents at some locations.

The addition of stratification to the model radically changed the super-inertial semidiurnal tidal current field. The stratified model produced surface currents with spatial variability and amplitude range comparable to what was derived from HF radar surface-current measurements, but the point-by-point comparisons are not favorable. Likewise, the subsurface current comparisons, performed at four deepwater locations, show considerable model-data differences. In future work, it will be important to try to learn how much of these differences are due to the simplified stratification used in the model runs considered here.

The model K_1 period (sub-inertial at this latitude) surface currents are not greatly affected by the addition of stratification. In some parts of the model domain, they agree quite well with the measured surface currents, but in other areas the observed currents are much stronger. This is thought to be due to the influence of diurnal period meteorological forcing on the real ocean, which is not included in the model forcing.

With the push towards real-time coastal ocean observing/modeling systems, the inclusion of tides with other forcing mechanisms will become more commonplace in nested data-assimilating primitive equation ocean models. It is our hope that this work highlights some of the issues to be addressed in validating those efforts.

Acknowledgements

Appendix A

The ICON model uses the mode splitting technique, where the separation of vertically integrated governing equations (barotropic, external mode) and the equations governing vertical structure (baroclinic, internal mode) is introduced. Boundary conditions are formulated for the barotropic and baroclinic modes separately and then adjusted to take into account the different truncation errors for those modes (Blumberg and Mellor, 1987). The barotropic vertically averaged velocities on the open boundary of the ICON model are determined from the following Flather (1976) condition:

$$\overline{u_n} = \overline{u_n^o} + (g/H)^{1/2}(\eta - \eta^o) \tag{2}$$

with

$$\overline{u_n^o} = \overline{u}_{\text{tide}}, \quad \eta^o = \eta_{\text{tide}} \tag{3}$$

where H is the water depth on the open boundary, g the gravitational acceleration, $\overline{u_n}$ the model vertically averaged outward normal component of velocity on the open boundary, η the ICON model sea-surface elevation calculated from the model continuity equation and located half a grid interval inside of the open boundary in the model domain, η_{tide} and $\overline{u_{tide}}$ are tidal sea-surface and vertically averaged tidal velocity, respectively, predicted by using the tidal constants for eight tidal constituents $(M_2, S_2, N_2, K_2, K_1, O_1, P_1, Q_1)$ from the OSU tidal model (Egbert and Erofeeva, 2002). These tidal constants are used to predict η_{tide} and $\overline{u_{tide}}$ using the Schwiderski (1980) scheme, which does not include a correction for the nodal factor (and uses 1 January 1975 as the time reference). The OSU model-derived amplitudes and phases for transports were rotated into the ICON curvilinear coordinates according to Paul Martin's scheme (personal comm.). The transport component orthogonal to the open boundary at each grid point was divided by the ICON bathymetry at that point to get the normal velocity $\overline{u_{tide}}$ used in the Flather condition (2).

The Flather condition represents a radiation condition on differences between the ICON model and the OSU model-derived sea-surface elevation and transports. It specifies the ICON model open-boundary velocity based on the model-derived sea-surface elevation and the SSH and transport from the OSU model. The Flather condition has been used by many researchers to force tidal models (e.g., Davies et al., 1997). When $\overline{u_n^o} = 0$ in (2), then the Flather condition becomes the condition introduced by Reid and Bodine (1968). In this case, the model open-boundary velocity is specified by using the model sea-surface elevation and the OSU model-derived sea-surface elevation (OSU model-derived transport is not used). Both of the above open-boundary conditions for the barotropic mode were tried in this study.

Barotropic tides propagating into the model domain will interact with the bathymetry and stratification and generate internal waves traveling toward open boundaries. For the baroclinic mode, the ideal open-boundary condition would let internal waves generated inside of the ICON model domain propagate out of the domain. Unfortunately, there is no existing radiative open-boundary condition that will let every internal wave radiate out of the model domain without reflection. Decomposition of variables in terms of vertical internal modes is a rather complicated problem in the case of varying depth and stratification on the open boundary. For this reason, the radiation condition with some estimate of only the first baroclinic mode is usually used. In our study, the following baroclinic open-boundary condition was used:

$$\frac{\partial u_n}{\partial t} + C_i \frac{\partial u_n}{\partial n} = 0 \qquad (4)$$

where u_n is the outward normal component of velocity on the open boundary, and C_i is the fixed baroclinic internal wave phase speed, $C_i = (0.001gH)^{1/2}$. Radiation condition (4) has been used by many researchers. For example, Oey and Chen (1992) reported relative insensitivity to the values of C_i if it is not too different from the phase speed of the first baroclinic mode.

Appendix B

Based on previous stratified applications of POM for tidal modeling by Cummins and Oey (1997), who found that 5 d was sufficient to establish equilibrium for the tide, and Cummins et al. (2001) who used a 20-d spin-up to simulate the internal tide generated at the Aleutian Ridge in the North Pacific, we thought that 22 d would be sufficient for the tidal response to reach equilibrium. We note, however, that for their simulation of the barotropic tides in the South Atlantic Bight, Blanton et al. (2004)

ran ADCIRC-2DDI (Luettich et al., 1992) for 180 d, and performed harmonic analysis on the last 90 d only. So initially, we chose to run the model for 56 d, ramping up the forcing over the first 7 d, and performing tidal analysis on the last 34 d. By the time we discovered that the difference between model and predicted (from NOS tidal constants) SSH continued to decrease over the first week of the analyzed time period, it was not feasible for a number of reasons, including the arrival of Hurricane Katrina, to redo all the model runs for a longer time period. Fortunately, the influence of the first 7 d in the 380-d analyzed time series from the 402-d run is minimal, and it is small even in the shorter runs.

The 34-d record length slightly exceeds the 29 d required to resolve six of the eight forcing constituents, but is well short of the 183 d needed to resolve all eight (with a Rayleigh criteria of one). The inference parameters, derived from measured sea level, were used in the tidal analysis of both SSH and velocity. While we might expect the relationship between tidal constituents to be the same for barotropic currents as for SSH, it is not at all clear that the same relationships should hold for the baroclinic currents. Hence, in the semidiurnal band, we focused primarily on the M_2 constituent, which is not involved in inference. Analysis of the initial model runs showed fairly large discrepancies between the observed and modeled K_1 currents, so to eliminate the possibility that inappropriate parameters were being used to infer the P_1 constituent from the K_1, a long (402-d) model run was done just for the case with stratification and the Flather boundary condition. We found that the tidal current ellipses calculated from the shorter model run (1) were almost indistinguishable from those from the longer model run (5), thus also demonstrating that the spin-up effects are small even for the shorter model run.

We have some evidence that the inference parameters applied in analysis of the shorter model runs, are appropriate for the barotropic currents, as well as the SSH. The model forcing has P_1/K_1 and K_2/S_2 relationships consistent with actual sea level. Using the last 380 d of model run 5, we verified that both the P_1/K_1 and K_2/S_2 amplitude ratios for SSH and surface currents (judged by the ellipse major axes), and the K_1-P_1 and S_2-K_2 SSH phase differences, varied very little over the model domain, and they agreed well with those expected from observed sea level and the boundary forcing. Given the variability in ellipse orientation and sense of rotation, surface-current ellipse phase differences were quite variable, and although most major axis ratios were close to the SSH values, there was a much wider range of values for the currents than for the SSH, including some areas where the ratio exceeded one. This would indicate that at least in the stratified case, nonlinear interactions could be transferring energy from the K_1 to the P_1 frequency. For most of the depth-averaged measured current records greater than 183 d in length, the P_1/K_1 and K_2/S_2

Table 6
Inference parameters derived from sea-level records (top line) were used for all inference

	P_1/K_1	K_1-P_1 (°)	K_2/S_2	S_2-K_2 (°)
Sea level	0.31	3.5	0.28	9.0
P2	0.33	−4.5	0.29	1.8
P3	0.32	4.1	0.24	22.5
Hopkins	0.47	−24.9	0.33	*−70.0
Sand hill	0.33	−18.1	0.37	37.9
Terrace Pt	0.33	−4.9	0.18	*59.3
M0	0.23	−21.7	0.39	−46.8

Amplitude ratios of major axes, and phase differences, calculated from depth-averaged current records greater than 200 d long are shown for comparison. Due to the 180° phase ambiguity in the current ellipses (since both phase and orientation can be flipped by 180°), there is a 180° uncertainty in the phase differences. Phase differences preceded by an asterisk have been adjusted by 180°.

amplitude ratios were in very good agreement with the inference ratios derived from the sea-level analyses (Table 6). Major axis ratios for surface-current ellipses derived from HF radar measurements for the constituents involved in inference show much more variability. Foreman et al. (1995) suggest that if the amplitude ratios do not match the tidal potential ratios, it is evidence that the tidal constants vary over the analysis period, which is an indication that these may not be reflective of barotropic processes.

References

Alford, M.H., 2003. Redistribution of the energy available for ocean mixing by long-range propagation of internal waves. Nature 423, 159–162.

Baines, P.G., 1986. Internal tides, internal waves and near-inertial motions. In: Mooers, C.N.K. (Ed.), Baroclinic Processes on Continental Shelves, Coastal Estuarine Series, vol. 3. AGU, Washington, DC, pp. 19–31.

Blanton, B.O., Werner, F.E., Seim, H.E., Luettich, R.A., Lynch, D.R., Smith, K.W., Voulgaris, G., Bingham, F.M., Way, F., 2004. Barotropic tides in the South Atlantic Bight. Journal of Geophysical Research 109, C12024.

Blumberg, A.F., Mellor, G.L., 1987. A description of a three-dimensional coastal ocean circulation model. In: Heaps, N.S. (Ed.), Three-Dimensional Coastal Ocean Models, Coastal Estuarine Series, vol. 4. AGU, Washington, DC, pp. 1–16.

Carter, G.S., Gregg, M.C., 2002. Intense, variable mixing near the head of Monterey Submarine Canyon. Journal of Physical Oceanography 32, 3145–3165.

Carter, G.S., Gregg, M.C., Lien, R.-C., 2005. Internal waves, solitary waves, and mixing on the Monterey Bay shelf. Continental Shelf Research 25, 1499–1520.

Chereskin, T.K., 1995. Direct evidence for an Ekman balance in the California Current. Journal of Geophysical Research 100, 18261–18269.

Chereskin, T.K., Morris, M.Y., Niiler, P.P., Kosro, P.M., Smith, R.L., Ramp, S.R., Collins, C.A., Musgrave, D.L., 2000. Spatial and temporal characteristics of the mesoscale circulation of the California Current from eddy-resolving moored and shipboard measurements. Journal of Geophysical Research 105, 1245–1269.

Crawford, W.R., Thomson, R.E., 1984. Diurnal-period continental shelf waves along Vancouver Island: a comparison of observations with theoretical models. Journal of Physical Oceanography 14, 1629–1646.

Cummins, P.F., Oey, L.-Y., 1997. Simulation of barotropic and baroclinic tides off northern British Columbia. Journal of Physical Oceanography 27, 762–781.

Cummins, P.F., Cherniawsky, J.Y., Foreman, M.G.G., 2001. North Pacific internal tides from the Aleutian Ridge: altimeter observations and modeling. Journal of Marine Research 59, 167–191.

Cummins, P.R., Masson, D., Foreman, M.G.G., 2000. Stratification and mean flow effects on diurnal tidal currents off Vancouver Island. Journal of Physical Oceanography 30, 15030.

Davies, A.M., Xing, J., 1995. An intercomparison and validation of a range of turbulence closure schemes used in three dimensional tidal models. In: Lynch, D.R., Davies, A.M. (Eds.), Quantitative Skill Assessment for Coastal Ocean Models. Coastal and Estuarine Studies Series. AGU, Washington, DC, pp. 71–95, 510pp.

Davies, A.M., Kwong, S.C.M., Flather, R.A., 1997. A three-dimensional model of diurnal and semidiurnal tides on the European shelf. Journal of Geophysical Research 102, 8625–8656.

Egbert, G.D., Erofeeva, S.Y., 2002. Efficient inverse modeling of barotropic ocean tides. Journal of Atmospheric and Oceanic Technology 19, 183–204.

Emery, W.J., Thomson, R.E., 1997. Data Analysis Methods in Physical Oceanography. Pergamon, Elsevier Science, New York, NY, 634pp.

Erofeeva, S.Y., Egbert, G.D., Kosro, P.M., 2003. Tidal currents on the central Oregon shelf: models, data, and assimilation. Journal of Geophysical Research 108, 3148.

Faller, A.J., Kaylor, R., 1969. Oscillatory and transitory Ekman boundary layers. Deep-Sea Research 16, 45–58.

Flather, R.A., 1976. A tidal model of the northwest European continental shelf. Memorie Societa Real Scienze Liege 6, 141–164.

Foreman, M.G.G., 1977. Manual for Tidal Heights Analysis and Prediction. Pacific Marine Science Report 77-10. Institute of Ocean Sciences, Patricia Bay, Sidney, BC, 97pp.

Foreman, M.G.G., 1978. Manual for Tidal Currents Analysis and Prediction. Pacific Marine Science Report 78-6. Institute of Ocean Sciences, Patricia Bay, Sidney, BC, 57pp.

Foreman, M.G.G., Thomson, R.E., 1997. Three-dimensional model simulations of tides and buoyancy currents along the west coast of Vancouver Island. Journal of Physical Oceanography 27, 1300–1325.

Foreman, M.G.G., Crawford, W.R., Marsden, R.F., 1995. De-tiding: theory and practice. In: Lynch, D.R., Davies, A.M. (Eds.), Quantitative Skill Assessment for Coastal Ocean Models. Coastal and Estuarine Studies Series. AGU, Washington, DC, pp. 203–239, (510pp).

Holloway, P.E., 2001. A regional model of the semidiurnal internal tide on the Australian North West Shelf. Journal of Geophysical Research 106, 19625–19638.

Huthnance, J.M., 1978. On coastal trapped waves: analysis and numerical calculation by inverse iteration. Journal of Physical Oceanography 8, 74–92.

Jachec, S.M., Fringer, O.B., Gerritsen, M.G., Street, R.L., 2006. Numerical simulation of internal tides and the resulting energetics within Monterey Bay and the surrounding area. Geophysical Research Letters 33, L12605.

Kindle, J.C., Hodur, R., deRada, S., Paduan, J., Rosenfeld, L., Chavez, F., 2003. A COAMPS^{TM} reanalysis for the Eastern Pacific: properties of the diurnal sea breeze along the central California coast. Geophysical Research Letters 29 (24).

Kunze, E., Rosenfeld, L.K., Carter, G.S., Gregg, M.C., 2002. Internal waves in Monterey Submarine Canyon. Journal of Physical Oceanography 32, 1890–1913.

Kurapov, A.L., Egbert, G.D., Allen, J.S., Miller, R.N., Erofeeva, S.Y., Kosro, P.M., 2003. The M_2 internal tide off Oregon: inferences from data assimilation. Journal of Physical Oceanography 33, 1733–1757.

Lazanoff, S.M., 1971. An evaluation of a numerical water elevation and tidal current prediction model applied to Monterey Bay. M.S. Thesis, Naval Postgraduate School, Monterey, CA.

Lien, R.C., Gregg, M.C., 2001. Observations of turbulence in a tidal beam and across a coastal ridge. Journal of Geophysical Research 106, 4575–4591.

Luettich, R.A., Westerink, J.J., Scheffner, N.W., 1992. ADCIRC: an advanced three-dimensional circulation model for shelves, coasts and estuaries; report 1: theory and methodology of ADCIRC-2DDI and ADCIRC-3DL. Technical Report DRP-92-6, Coastal Engineering Research Center, US Army Engineering Waterways Experimental Station, Vicksburg, MS.

Mellor, Yamada, 1982. Development of a turbulence closure model for geophysical fluid problems. Reviews of Geophysics and Space Physics 20, 851–875.

Noble, M., Rosenfeld, L.K., Smith, R.L., Garnder, J.V., Beardsley, R.C., 1987. Tidal currents seaward of the northern California continental shelf. Journal of Geophysical Research 92, 1733–1744.

NOS, A., 2000. Tide and Current Glossary. NOAA, Silver Spring, MD, 34pp. Available at ⟨http://tidesandcurrents.noaa.gov/publications/glossary2.pdf⟩.

Oey, L.-Y., Chen, P., 1992. A model simulation of circulation in the north-east Atlantic shelves and seas. Journal of Geophysical Research 97, 20087–20115.

Paduan, J.D., Cook, M.S., 1997. Mapping surface currents in Monterey Bay with CODAR-type HF radar. Oceanography 10, 49–52.

Paduan, J.D., Rosenfeld, L.K., 1996. Remotely sensed surface currents in Monterey Bay from shore-based HF radar (Coastal Ocean Dynamics Application Radar). Journal of Geophysical Research 101, 20669–20686.

Paduan, J.D., Shulman, I., 2004. HF radar data assimilation in the Monterey Bay area. Journal of Geophysical Research 109, C07S09.

Park, J.-H., Watts, D.R., 2006. Internal tides in the southwestern Japan/East Sea. Journal of Physical Oceanography 36, 22–34.

Pawlowicz, R., Beardsley, R., Lentz, S., 2002. Classical tidal harmonic analysis including error estimates in MATLAB using T_TIDE. Computers and Geosciences 28, 929–937.

Pereira, A.F., Beckmann, A., Hellmer, H.H., 2002. Tidal mixing the southern Weddell Sea: results from a three-dimensional model. Journal of Physical Oceanography 32, 2151–2169.

Petruncio, E.T., 1993. Characterization of tidal currents in Monterey Bay from remote and in-situ measurements. M.S. Thesis, Naval Postgraduate School, Monterey, CA, 113pp.

Petruncio, E.T., Rosenfeld, L.K., Paduan, J.D., 1998. Observations of the internal tide in Monterey Canyon. Journal of Physical Oceanography 28, 1873–1903.

Petruncio, E.T., Paduan, J.D., Rosenfeld, L.K., 2002. Numerical simulations of the internal tide in a submarine canyon. Ocean Modelling 4, 221–249.

Price, J.F., Weller, R.A., Pinkel, R., 1986. Diurnal cycling: observations and models of the upper ocean response to diurnal heating, cooling, and wind mixing. Journal of Geophysical Research 91, 8411–8427.

Rainville, L., Pinkel, R., 2006. Propagation of low-mode internal waves through the ocean. Journal of Physical Oceanography 36, 1220–1236.

Ramp, S.R., Rosenfeld, L.K., Tisch, T.D., Hicks, M.R., 1997. Moored observations of the current and temperature structure over the continental slope off central California. Part I: a basic description of the variability. Journal of Geophysical Research 102, 22877–22902.

Ramp, S.R., Paduan, J.D., Shulman, I., Kindle, J., Bahr, F.L., Chavez, F., 2005. Observations of upwelling and relaxation events in the northern Monterey Bay during August 2000. Journal of Geophysical Research 110, C07013.

Reid, R.O., Bodine, B.R., 1968. Numerical model for storm surges in Galveston Bay. ASCE, Journal of the Waterways Harbors Division 94, 33–57.

Rosenfeld, L.K., 1987. Tidal band current variability over the northern California continental shelf. Ph.D. Dissertation, Technical Report WHOI-87-11. Joint Progress in Oceanography, Woods Hole Oceanographic, Institute/Massachusetts Institute of Technology, Woods Hole, MA, 237pp.

Rosenfeld, L.K., 1988. Diurnal period wind stress and current fluctuations over the continental shelf off northern California. Journal of Geophysical Research 93, 2257–2276.

Rosenfeld, L.K., Schwing, F., Garfield, N., Tracy, D.E., 1994. Bifurcated flow from an upwelling center: a cold water source for Monterey Bay. Continental Shelf Research 14, 931–964.

Rosenfeld, L.K., Paduan, J.D., Petruncio, E.T., Goncalves, J.E., 1999. Numerical simulations and observations of the internal tide in a submarine canyon. In: 11th 'Aha Huliko'a Hawaiian Winter Workshop, Honolulu, HI, January 1999, pp. 63–71.

Schomaker, C.W., 1983. A model for tidal circulation adapted to Monterey Bay, California. M.S. Thesis, Naval Postgraduate School, Monterey, CA.

Schwiderski, E.W., 1980. On charting global ocean tides. Review of Geophysics and Space Physics 18, 243–268.

Shulman, I., Paduan, J.D., 2008. Assimilation of HF radar-derived radials and total currents in the Monterey Bay area. Deep-Sea Research II, this issue [doi:10.1016/j.dsr2.2008.08.004].

Shulman, I., Wu, C.-R., Lewis, J.K., Paduan, J.D., Rosenfeld, L.K., Kindle, J.C., Ramp, S.R., Collins, C.A., 2002. High resolution modeling and data assimilation in the Monterey Bay area. Continental Shelf Research 22, 1129–1151.

Smagorinsky, J., 1963. General circulation experiments with the primitive equations, I. The basic experiment. Monthly Weather Review 91, 99–164.

Strub, P.T., James, C., 2000. Altimeter-derived variability of surface velocities in the California Current System: 2. Seasonal circulation and eddy statistics. Deep-Sea Research 47, 831–870.

Tennekes, H., Lumley, J.L., 1972. A First Course in Turbulence. The MIT Press, Cambridge, MA, 300pp.

Wang, X., Chao, Y., Dong, C., Farrara, J., Li, Z., McWilliams, J.C., Paduan, J.D., Rosenfeld, L.K., 2008. Modeling tides in Monterey Bay, California. Deep-Sea Research II, this issue [doi:10.1016/j.dsr2.2008.08.012].

Xing, J., Davies, A.M., 1998a. A three-dimensional model of internal tides on the Malin–Hebrides shelf and shelf edge. Journal of Geophysical Research 103, 27821–27847.

Xing, J., Davies, A.M., 1998b. Influence of stratification upon diurnal tidal currents in shelf edge regions. Journal of Physical Oceanography 28, 1803–1831.

Xu, J.P., Noble, M.A., Eittreim, S.L., Rosenfeld, L.K., Schwing, F.B., Pilskaln, C.H., 2002. Distribution and transport of suspended particulate matter in Monterey Canyon, California. Marine Geology 181, 215–234.